Check for updates

ADVANCED FUNCTIONAL MATERIALS
www.afm-journal.de

SMaRT Stacking: A Methodology to Produce Optimally Layered EMI Shields with Maximal Green Index Using Fused Deposition Modeling

*Stijn De Smedt, Brecht Evens, Pramod Ravichandran, Panagiotis Patrinos, Frederik Van Loock, and Ruth Cardinaels**

Effective electromagnetic interference (EMI) shielding requires structures that are both highly effective and absorption-dominant, qualities that are often in conflict. Achieving strong shielding typically comes at the expense of secondary electromagnetic pollution, as most conventional shields reflect incoming waves rather than absorbing them. To address this issue, current research is shifting toward asymmetrically layered and gradient multilayer shields, aiming to achieve both high shielding and strong absorption. However, no systematic method exists to determine the layer ordering that maximizes absorption for a given set of materials, and contemporary EMI shields still rely heavily on expert intuition and trial-and-error approaches. This work proposes a generalizable optimization method based on gray-box modeling techniques from system identification to design the optimal stacking sequence of ten additively manufactured layers, producing a 4 mm thick, absorption-dominant EMI shield for the X-band. Using fused deposition modeling (FDM) to process polylactic acid (PLA) with varying loadings of multiwalled carbon nanotubes (MWCNT), shields are fabricated with optimized layer orders tailored to different shielding requirements. To illustrate, the resulting EMI shields demonstrate exceptionally high absorption while maintaining high overall shielding performance. A green index, or absorption to reflection ratio, ≈100 is obtained for the optimal layer order requiring 25 dB of shielding.

1. Introduction

The omnipresence of electromagnetic (EM) waves in modern society is undeniable. From mobile communication and missile detection to medical devices and even playing a song via Bluetooth, countless technologies depend on the emission and reception of EM waves. However, EM waves are not without drawbacks. Because they can interact with each other and with materials, including human tissue, they can cause damage and malfunctions ranging from scatter on the radio, errors in devices or failure of electronic components to automatic nuclear reactor shutdowns or possible health effects in human beings.[1–4] Clearly, protection against unwanted EM radiation, also known as electromagnetic interference (EMI), is needed.[5] The most effective EMI shields consist of thin sheets of highly conductive metals, which can for example be placed around sensitive electronic components, and reflect almost all incoming EM signals. However effective these are, they create another problem of (secondary) EM pollution, placing nearby components and organisms at risk due to their reflection based shielding. The dominant shielding mechanism is indicated by the green index, or absorption to reflection ratio (A/R) while the shielding effectiveness SE expresses the overall shielding performance of the shield.[6] A recent review emphasizes the need for polymer-based asymmetric absorption-dominant green EMI shields.[7] The reflection and transmission of energy should be minimized while maximally

S. De Smedt, P. Ravichandran, R. Cardinaels
Soft Matter, Rheology and Technology (SMaRT), Department of Chemical Engineering
KU Leuven
Heverlee 3001, Belgium
E-mail: ruth.cardinaels@kuleuven.be

The ORCID identification number(s) for the author(s) of this article can be found under https://doi.org/10.1002/adfm.202512713

B. Evens, P. Patrinos
ESAT - STADIUS Department of Electrical Engineering
KU Leuven
Heverlee 3001, Belgium

F. Van Loock, R. Cardinaels
Processing and Performance of Materials, Department of Mechanical Engineering
TU Eindhoven
Eindhoven 5600 MB, The Netherlands

© 2025 The Author(s). Advanced Functional Materials published by Wiley-VCH GmbH. This is an open access article under the terms of the Creative Commons Attribution License, which permits use, distribution and reproduction in any medium, provided the original work is properly cited.

DOI: 10.1002/adfm.202512713

converting the incoming EM energy to heat to obtain green shielding. Recent work on bilayer and multilayer structures has shown the potential of layered EMI shields and yielded valuable insights in their performance.[8,9] However, it is not straightforward to determine which asymmetric structure would be the best solution for certain shielding requirements or applications.

Many researchers devote their time designing novel and more performant EMI shields using new material formulations, for example by incorporating functional fillers such as for instance multiwalled carbon nanotubes (MWCNT) in a polymer matrix,[10,11] or by using manufacturing techniques like multi-material additive manufacturing[12] or additive manufacturing with 3D printed multi-material filaments to obtain spatial control of material properties.[13] While the transition of metal-based to polymer composite based EMI shields is going fast, there is no structural approach yet to determine the optimal distribution of fillers throughout an EMI shielding structure. The most well known multilayered shields are sandwich structures, which relate to so-called microwave absorbers or radar absorbing materials (RAMs)[14] and A-B multilayers.[8] In the field of RAMs, the return loss (RL) is often reported, which represents the ratio of the reflected power to the incident power on the shield and can be related to the absorption inside the shield because a perfect reflector is placed just behind the RAM, so that all energy which would be transmitted is reflected back to the front of the shield. A metal shield would consequently show a RL close to 0 dB since no energy is lost inside the material and the whole wave is nearly fully reflected. For real materials, RL values in absolute value greater than 10 dB correspond to 90% absorption and thus a green index greater than 9. Note that for these measurements, the EM wave passes twice through the shield because of the reflector, once in the incoming direction and once in the opposite direction when it is reflected back to the front of the shield, such that its traveled distance in the absorber material is double the thickness of the shield.[15] For RAMs ranging from 5 mm to over 30 mm in thickness, values of RL ranging from –23 to –58 dB, which corresponds to A/R ratios of 13 to 768 respectively, are reported for various frequency ranges.[14–16] The manufacturing of these RAM shields is often cumbersome and their absorption bandwidth can be very narrow, sometimes only targeting a very specific frequency.[17] Other multilayer structures often perform very well in shielding effectiveness but lack in green index. Values reported for A-B multilayer structures with thicknesses of several millimeters range from a few decibels to over 70 dB in the X-band with green indices not surpassing one.[8,9] Although such studies provide valuable insights, they primarily rely on expert knowledge and iterative experimentation to achieve the desired shielding effectiveness.[18] By using multiple material compositions, the response of the wave within the shield can be spatially tuned and is not limited to only two material responses but layers can be placed such that a synergy between consecutive layers increases the absorption and total shielding performance. In this respect, gradient structures are a promising candidate to increase the absorption of a multilayer structure, achieving higher absorption in general than isotropic shields.[19,20] Such shields are reported to obtain green indices ranging from 0.5 to ≈1. However, they often obtain lower total shielding effectiveness or a smaller frequency range in which absorption dominant shielding is obtained.[21]

This work aims to move beyond expert-driven and straightforward designs such as A-B multilayer and gradient shields by developing a systematic approach to EMI shield optimization. In particular, rather than relying on trial and error, we learn a predictive model of the multilayered shield from data and subsequently use an optimization framework to determine the optimal layer stacking, ensuring the highest A/R ratio for a required shielding effectiveness. A key challenge in this process is sample efficiency: How can we learn a sufficiently accurate predictive model of the multilayered shield using only a limited number of samples? To address this, we take a model-based approach. In an ideal scenario, the physical laws governing EM field propagation give accurate predictions for the shielding behavior,[22] given knowledge of the material properties, specifically permittivity and permeability. Therefore, instead of treating the entire predictive model as a black box, we parametrize the materials in terms of their permittivity and permeability and learn their parameters from data. This idea is known as gray box modeling in system identification[23] and ensures that our approach remains sample-efficient while adhering to fundamental physical principles. Note that our approach is closely related to model-based reinforcement learning,[24] where one alternates between system identification and planning steps. More broadly, learning model parameters is also closely related to learning the parameters of neural networks.[25] However, note that our framework differs from so-called physics-informed neural networks (PINNs),[26] as we incorporate physical dynamics directly into the model structure, whereas PINNs enforce physics through an error term in the loss function.

Throughout this paper, we provide a design methodology for additively manufactured layered EMI shields, interchangeably called stacks, of 4 mm in thickness using fused deposition modeling (FDM) of polylactic acid (PLA) nanocomposites with different loadings of MWCNTs as the production method. The choice for this material system is twofold. On the one hand, (PLA) is the most used polymer in FDM and on the other hand, MWCNTs are a frequently used filler due to their high aspect ratio and low percolation threshold for electrical conductivity.[11,27] As a demonstrator for this methodology, we design multilayers with shielding effectiveness above 20 dB in the X-band, where satellite communication and defense tracking among other applications operate, while maximizing absorption. Absorption-dominant EMI shields, with a green index of at least 1, meaning that at least the same amount of energy is absorbed as reflected, can have a large impact in this frequency range. Based on the learned model parameters for different PLA/MWCNT nanocomposites, layer orders are predicted which maximize the absorption while maintaining a required value of SE. Using this approach we show unprecedented high absorption for 10 composite layers in a 4 mm multilayer EMI shield.

2. Theoretical Framework of Multilayer Shielding

When an EM wave encounters a material other than the medium it is traveling in, it can interact with this material via three mechanisms, namely reflection, absorption and transmission. Depending on the material properties, quantified by the relative dielectric permittivity ϵ and relative magnetic permeability μ, these mechanisms can be more or less pronounced.[22,28] For a shield which

© 2025 The Author(s). Advanced Functional Materials published by Wiley-VCH GmbH

16163028, 0, Downloaded from https://advanced.onlinelibrary.wiley.com/doi/10.1002/adfm.202512713 by Ku Leuven, Wiley Online Library on [23/09/2025]. See the Terms and Conditions (https://onlinelibrary.wiley.com/terms-and-conditions) on Wiley Online Library for rules of use; OA articles are governed by the applicable Creative Commons License

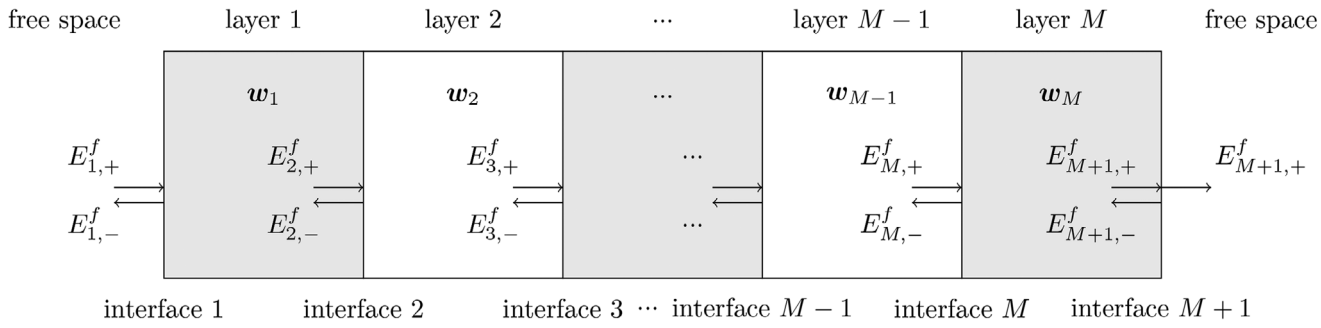


Figure 1. Visualization of the multilayer dielectric shield.

is uniform in composition, part of the incoming wave's energy reflects at the front face of the shield due to the impedance mismatch between the shield and the medium the wave is traveling in, which is mostly air. The rest of the energy is able to enter the shield's body where it can be dissipated, or absorbed, by interaction with conductive or magnetic particles. On the rear side of the shield, the remaining energy can reflect back into the shield or can leave the shield as transmission.[29] **Figure 1** gives a schematic representation of these mechanisms in a multilayer structure where at each interface part of the incoming wave can be reflected and absorption can take place in each layer. To create an effective EMI shield, transmission should be low. This is often expressed in a requirement of at least 25 to 30 dB of total shielding effectiveness (SE). This means that only 0.1% to 0.3% of the incoming energy can travel through the shield. Moreover, to prevent secondary EM pollution, the reflection of energy should be minimal, which means that absorption should be the primary shielding mechanism. Based on these physical mechanisms, a simple mathematical model can be constructed which computes the shielding performance of a multilayer EMI shield given the material properties of each layer.[22] Since the material properties are also determined by the way in which the material is processed and stacked together, rather than determining the permittivity and permeability via conventional methods such as the Nicolson–Ross–Weir[30] algorithm, we propose in Section 3.1 to learn this material function from data on multilayer stacks. Moreover, once this model is obtained, it is used to predict the most absorbing sequence of a number of layers in an EMI shield of a given thickness for a specified minimal SE. The working principle of this optimization is clarified in Section 3.

Consider a multilayer dielectric layered structure consisting of M layers, $M+1$ interfaces and $M+2$ dielectric media, where the outer two media correspond to free space and the layers are infinitely wide, as illustrated in Figure 1.[22] Each layer of thickness $t>0$ is indexed by $i \in [1,\dots,M]$. We assume that the complex relative permittivity ε and the complex relative permeability μ of each layer i can be obtained as a function of the material composition used in layer i, represented using a vector $\boldsymbol{w}_i \in \mathbb{R}^{n_x}$. In this particular case, $\boldsymbol{w}_i$ denotes the MWCNT loading in a layer as the weight fraction of filler so that $\boldsymbol{w}_i = w\%$. For convenience, we denote the material properties of all M layers using a single vector $\boldsymbol{w} = (\boldsymbol{w}_1,\dots,\boldsymbol{w}_M) \in \mathbb{R}^{Mn_x}$. We will discuss how we can learn such functions ε and μ from measurement data on multilayer stacks in Section 3.1, for now, suppose these functions are given. Then, the characteristic impedance of layer i is given by $\eta(\boldsymbol{w}_i) = \sqrt{\frac{\mu(\boldsymbol{w}_i)}{\epsilon(\boldsymbol{w}_i)}}$[22] and at each interface $i \in [1,\dots,M+1]$, the reflection coefficient from the left of the interface is given by[22]

$$\rho(\boldsymbol{w}_{i-1},\boldsymbol{w}_i) = \begin{cases} \frac{\eta(\boldsymbol{w}_1)-1}{\eta(\boldsymbol{w}_1)+1}, & \text{if } i=1, \\ \frac{1-\eta(\boldsymbol{w}_M)}{1+\eta(\boldsymbol{w}_M)}, & \text{if } i=M+1, \\ \frac{\eta(\boldsymbol{w}_i)-\eta(\boldsymbol{w}_{i-1})}{\eta(\boldsymbol{w}_i)+\eta(\boldsymbol{w}_{i-1})}, & \text{otherwise,} \end{cases} \tag{1}$$

where we use that the medium on the left and the right of the shield is air (free space). Moreover, denoting the permittivity and permeability of vacuum by ε_0 and μ_0, the refractive index of layer i is then given by $n(\boldsymbol{w}_i) = \sqrt{\frac{\varepsilon(\boldsymbol{w}_i)\mu(\boldsymbol{w}_i)}{\epsilon_0\mu_0}}$. Note that in our results section, we will consider non-magnetic materials, for which μ is equal to one.

Consider a wave traveling through the multilayer dielectric structure from left to right with a certain frequency f expressed in Hz. Assume that there is no backward field in the rightmost medium and denote the forward field in the rightmost medium by $E^f_{M+1,+} \in \mathbb{C}$. We denote the forward field at the left of interface i by $E^f_{i,+} \in \mathbb{C}$, and analogously, we denote the backward field at the left of interface i by $E^f_{i,-} \in \mathbb{C}$. Further, denote the free-space wavenumber by $k^f_0 = \frac{2\pi f}{c_0}$, with c_0 the speed of light in free space. Then, it follows that for all $i \in [1,\dots,M]$ the fields propagate in the following manner:[22]

$$\begin{bmatrix} E^f_{i,+}(\boldsymbol{w}) \\ E^f_{i,-}(\boldsymbol{w}) \end{bmatrix} = \frac{1}{1+\rho(\boldsymbol{w}_{i-1},\boldsymbol{w}_i)} \begin{bmatrix} 1 & \rho(\boldsymbol{w}_{i-1},\boldsymbol{w}_i) \\ \rho(\boldsymbol{w}_{i-1},\boldsymbol{w}_i) & 1 \end{bmatrix} \begin{bmatrix} e^{jk^f_0 t n(\boldsymbol{w}_i)} & 0 \\ 0 & e^{-jk^f_0 t n(\boldsymbol{w}_i)} \end{bmatrix} \begin{bmatrix} E^f_{i+1,+}(\boldsymbol{w}) \\ E^f_{i+1,-}(\boldsymbol{w}) \end{bmatrix} \tag{2}$$

$$\begin{bmatrix} E^f_{M+1,+}(\boldsymbol{w}) \\ E^f_{M+1,-}(\boldsymbol{w}) \end{bmatrix} = \frac{1}{1+\rho(\boldsymbol{w}_M,\boldsymbol{w}_{M+1})} \begin{bmatrix} 1 \\ \rho(\boldsymbol{w}_M,\boldsymbol{w}_{M+1}) \end{bmatrix} E^f_{M+1,+} \tag{3}$$

For instance, when $M=1$, it can be shown that

© 2025 The Author(s). Advanced Functional Materials published by Wiley-VCH GmbH

16163028, 0, Downloaded from https://advanced.onlinelibrary.wiley.com/doi/10.1002/adfm.202512713 by Ku Leuven, Wiley Online Library on [23/09/2025]. See the Terms and Conditions (https://onlinelibrary.wiley.com/terms-and-conditions) on Wiley Online Library for rules of use; OA articles are governed by the applicable Creative Commons License

$$\Gamma^f(\boldsymbol{w}) = \frac{\rho(\boldsymbol{w}_0, \boldsymbol{w}_1)(1 - e^{-2jk_0^f tn(\boldsymbol{w}_1)})}{1 - \rho(\boldsymbol{w}_0, \boldsymbol{w}_1)^2 e^{-2jk_0^f tn(\boldsymbol{w}_1)}} \quad \text{and}$$

$$\mathcal{T}^f(\boldsymbol{w}) = \frac{(1 - \rho(\boldsymbol{w}_0, \boldsymbol{w}_1)^2) e^{-jk_0^f tn(\boldsymbol{w}_1)}}{1 - \rho(\boldsymbol{w}_0, \boldsymbol{w}_1)^2 e^{-2jk_0^f tn(\boldsymbol{w}_1)}} \tag{4}$$

The reflection response $\Gamma^f(\boldsymbol{w})$ is also known as the S_{11}-parameter and the transmission response $\mathcal{T}^f(\boldsymbol{w})$ is also known as the S_{21}-parameter. Note that these parameters can be measured in the EM characterization as described in Section 6.2 Characterization of PLA/MWCNT Nanocomposites. Using these quantities, we define the reflection coefficient $R^f_{\text{model}}(\boldsymbol{w})$, the transmission coefficient $T^f_{\text{model}}(\boldsymbol{w})$ and absorption coefficient $A^f_{\text{model}}(\boldsymbol{w})$ as

$$R^f_{\text{model}}(\boldsymbol{w}) = \left|\Gamma^f(\boldsymbol{w})\right|^2, \quad T^f_{\text{model}}(\boldsymbol{w}) = \left|\mathcal{T}^f(\boldsymbol{w})\right|^2 \quad \text{and}$$

$$A^f_{\text{model}}(\boldsymbol{w}) = 1 - R^f_{\text{model}}(\boldsymbol{w}) - T^f_{\text{model}}(\boldsymbol{w}) \tag{5}$$

Finally, we denote the SE in dB of the multilayer dielectric structure by

$$\text{SE}^f_{\text{model}}(\boldsymbol{w}) = 10 \log_{10}\left(\frac{1}{T^f_{\text{model}}(\boldsymbol{w})}\right) \tag{6}$$

Note that this formalism assumes EM waves traveling in free space through an infinitely wide plane and does not take into account effects introduced by the waveguide when the EM response of materials is measured.[31]

3. Optimization Methodology for Multilayered Shields

3.1. Learning the Permittivity and Permeability Functions

In this subsection, we introduce a practical methodology for learning an accurate complex permittivity function ϵ and complex permeability function μ from data using optimization.[32] Directly learning an arbitrary function mapping from data is generally intractable, as such mappings are infinite-dimensional while the available data is finite and limited. To address this challenge, our approach begins with a parametrization step. In particular, we propose to first introduce a class of parametrized functions $\epsilon(\boldsymbol{w}_i, p)$ and $\mu(\boldsymbol{w}_i, p)$ and then learn the parameters $p \in \mathbb{R}^{n_p}$ from data instead. For these parametrized functions, one can encode some expert knowledge to ease the learning process. For instance, depending on the expected behavior of the material, one can use for example linear functions, quadratic functions, logistic functions,[33] spline functions[34] or Gompertz functions.[35] Given these parametrized functions, the characteristic impedance of layer i is given by $\eta(\boldsymbol{w}_i, p) = \sqrt{\frac{\mu(\boldsymbol{w}_i, p)}{\epsilon(\boldsymbol{w}_i, p)}}$ and yields, by plugging this into Equations (1)–(6), a parametric model for the reflection coefficient $R^f_{model}(\boldsymbol{w}, p)$, the absorption coefficient $A^f_{model}(\boldsymbol{w}, p)$ and the shielding effectiveness $\text{SE}^f_{model}(\boldsymbol{w}, p)$.

Suppose that one has collected a training dataset consisting of S stacks, whereby every stack is denoted with an index $s \in [1, \dots, S]$ with corresponding vector $\boldsymbol{w}^s = (\boldsymbol{w}^s_1, \dots, \boldsymbol{w}^s_M)$, containing the weight fraction of filler in each layer. Corresponding measurements of the ratio between the absorption and reflection coefficients are then expressed by $A^f_{\text{exp,s}}/R^f_{\text{exp,s}}$ and the shielding effectiveness by $\text{SE}^f_{\text{exp,s}}$ at all frequencies $f \in \mathcal{V}$, where $\mathcal{V}$ denotes the discrete set of all tested frequencies. The relative error between two quantities $a, b \in \mathbb{R}$ is defined as $\text{e}_{\text{rel}}(a, b) = |a - b||b|$. Then, one can learn the optimal set of parameters $p \in \mathbb{R}^{n_p}$ by minimizing the sum of the relative errors between the measured and predicted A/R and SE, i.e., by solving

$$\underset{p \in \mathcal{P}}{\text{minimize}} \ \frac{1}{2S} \sum_{s=1}^{S} \sum_{f \in \mathcal{V}} \left[\text{e}_{\text{rel}}\left(\frac{A^f_{\text{model}}(\boldsymbol{w}^s, p)}{R^f_{\text{model}}(\boldsymbol{w}^s, p)}, \frac{A^f_{\text{exp,s}}}{R^f_{\text{exp,s}}} \right)^2 + \text{e}_{\text{rel}}\left(\text{SE}^f_{\text{model}}(\boldsymbol{w}^s, p), \text{SE}^f_{\text{exp,s}} \right)^2 \right] \tag{7}$$

where the set $\mathcal{P} \subseteq \mathbb{R}^{n_p}$ can be used to encode prior knowledge on the parameters p.

Our learning methodology differs significantly from the traditional Nicolson–Ross–Weir (NRW) method, which is designed to determine the complex permittivity and permeability of a *single* homogeneous material by solving the system in Equation (4), given measurements of the reflection and transmission response.[30] This measurement technique suffers from a well-known phase ambiguity problem, as this system has infinitely many solutions differing by multiples of 2π in phase. As a result, it does not extend naturally to materials with varying properties: applying it across samples and fitting a curve through the retrieved parameters can be unreliable, as the results depend heavily on arbitrary phase choices. In contrast, our learning-based approach infers parameterized models for permittivity and permeability that are consistent across samples. Since we aim to model materials with varying properties (unlike the NRW method), our methodology allows to use multilayer stacks as training data, which significantly enriches the dataset and improves the model's ability to generalize.

Note that the function to minimize in Equation (7) is generally highly nonconvex. To address this, we propose solving Equation (7) using the basin-hopping methodology.[36] This method aims to solve general nonconvex optimization problems with potentially many local minima through an iterative procedure. Starting from some initial guess, the method performs a random perturbation, from which a local optimizer is initialized, effectively hopping to a different basin in the optimization landscape. By repeatedly performing local optimizations and random perturbations, basin-hopping explores the optimization landscape, escaping local minima and increasing the likelihood of finding the global minimum. To solve the inner subproblems, we use sequential least squares programming, first introduced by Kraft et al.[37]

3.2. Optimizing the Shielding Properties of a Multilayered Shield

Having learned the permittivity and permeability functions describing the properties of the PLA/MWCNT materials, the goal is to design multilayer dielectric structures which maximize the

© 2025 The Author(s). Advanced Functional Materials published by Wiley-VCH GmbH

16163028, 0, Downloaded from https://advanced.onlinelibrary.wiley.com/doi/10.1002/adfm.202512713 by Ku Leuven, Wiley Online Library on [23/09/2025]. See the Terms and Conditions (https://onlinelibrary.wiley.com/terms-and-conditions) on Wiley Online Library for rules of use; OA articles are governed by the applicable Creative Commons License

ratio between the absorption and the reflection coefficient, while simultaneously ensuring a minimum shielding effectiveness, SE_{min}. To this end, we consider the following optimization problem:

$$\underset{\boldsymbol{w}_1,\ldots,\boldsymbol{w}_M \in \mathcal{W}}{maximize} \quad \left[\min_{f \in \mathcal{V}} \left\{ \frac{A^f_{model}(\boldsymbol{w})}{R^f_{model}(\boldsymbol{w})} \right\} \right] \quad \text{subject to} \quad SE_{min} \leq \min_{f \in \mathcal{V}} \left\{ SE^f_{model}(\boldsymbol{w}) \right\} \tag{8}$$

where $\mathcal{W}$ denotes the set of material properties which can be manufactured, which is assumed to be either a convex set (e.g. a range of material properties $\mathcal{W} = [\boldsymbol{w}_{min}, \boldsymbol{w}_{max}]$), or a discrete set of distinct material properties $\mathcal{W} = \{\boldsymbol{w}_{min}, \ldots, \boldsymbol{w}_{max}\}$.

Similar to problem in Equation (7), problem in Equation (8) is generally highly nonconvex due to the intricate behavior of the field propagating through the multilayer dielectric structure. If $\mathcal{W} = [\boldsymbol{w}_{min}, \boldsymbol{w}_{max}]$, the problem can be solved using the same basin-hopping algorithm as for problem in Equation (7). If $\mathcal{W} = \{\boldsymbol{w}_{min}, \ldots, \boldsymbol{w}_{max}\}$ (a discrete set with L different options), one could iterate over all L^M possible stacks and select the best one, i.e., solving the problem using brute-force. However, it should be clear that this quickly becomes intractable when the number of layers M and the number of options per layer L become too large.

Therefore, we propose a simple two-stage approach, significantly reducing the algorithmic complexity of the brute-force step. First, given an initial guess, we solve the problem over the continuous interval $[\boldsymbol{w}_{min}, \boldsymbol{w}_{max}]$ using the same method as for problem in Equation (7). Then, to find the best solution in the discrete set $\mathcal{W}$, we consider only the $\ell < L$ options for each layer which are closest to the continuous solution and perform a brute-force search over the resulting ℓ^M stacks. Of course, when ℓ is selected to be equal to one, this simply corresponds to finding the single discrete solution which is closest to the continuous solution. Typically, $\ell \approx 4$ to ensure that a performant discrete solution is achieved.

4. Results and Discussion

First, the rheological, thermal and EM characterization of all individual composites is reported in Section 4.1. These are of utmost importance when determining the additive manufacturing processing parameters of these materials. In Section 4.2 the EM properties of the composite stacks and the training of the permittivity function is covered. Using this knowledge, the algorithm can predict the optimal order of 10 layers in a 4 mm stack to maximally absorb the incoming EM energy. These stack designs and their shielding performance are discussed in Sections 4.3 and 4.4, respectively.

4.1. Thermal and Rheological Properties of PLA/MWCNT Nanocomposites

A collection of PLA/MWCNT nanocomposites of different MWCNT loadings are manufactured in the form of filaments for 3D printing and characterized as described in Section 6. The set of nanocomposite loadings is given by

$$\mathcal{W} = \{0.0,\ 0.5,\ 1.0,\ 2.5,\ 3.5,\ 5.0,\ 6.0,\ 7.5,\ 8.5,\ 10.0\} \tag{9}$$

Table 1. Thermal properties of PLA/MWCNT nanocomposites with w the loading of the composite, w_{res} the residue in TGA at 550°C, Δm_{90} the weight loss after 90 min at 190°C, T_d the degradation temperature and T_m the melting temperature.

w [wt%]	w_{res} [wt%]	Δm_{90} [wt%]	T_d[°C]	T_m[°C]
0.0	0.3±0.12	−1.6	369.7 ± 0.6	149.1± 1.4
0.5	1.2±0.19	—	366.5 ± 0.3	150.8±0.9
1.0	1.6±0.13	—	368.8±1.7	149.4±0.6
2.5	2.7±0.64	—	365.9± 0.4	152.1±0.7
3.5	3.4±0.27	—	365.0±0.8	151.1±0.3
5.0	5.4±0.24	−0.8	367.2±2.5	150.9±0.4
6.0	6.4±0.88	—	359.2±2.0	151.0±1.2
7.5	7.5±0.15	—	365.9±2.4	150.6±0.8
8.5	8.1±0.38	—	360.3±2.2	150.4±0.3
10.0	11.3±0.68	−1.1	360.9±2.1	150.6±0.1

The set of filament compositions is limited to a maximal loading of 10 wt% MWCNT in the PLA matrix because higher loadings resulted in a filament which was too brittle to process in Bowden tube or direct drive 3D printers. The relevant thermal properties to determine the parameters for the additive manufacturing process are given in **Table 1**. The residue mass w_{res} is a good check of the accuracy of the desired loading as well as the overall uniformity of the filaments. Since only the filler should remain after degradation, w_{res} should be close to w. The reported value of w_{res} is an average taken over at least three samples at random positions throughout the filament and agrees well with the desired loadings. The degradation temperatures T_d are found to be ≈365 °C, which poses an upper limit for the temperature of the printer nozzle. Since the melting temperature T_m of all materials is ≈150 °C, a printing temperature of 190 °C is chosen, which is in line with the conventional processing temperature in additive manufacturing of PLA. The mass loss after 90 min at 190 °C, Δm_{90}, is reported for three filament compositions and remains less than 2%. This assures that degradation can be neglected during the rheological measurements and additive manufacturing at 190 °C.

Figure 2 presents an overview of the relevant material characteristics for three selected filaments in $\mathcal{W}$, namely the pure PLA and filaments with 5.0 and 10.0 wt% MWCNT loadings, spanning the whole loading range. Each curve and each data point shown is the average of three measurements on different samples. The repeatability of the data is demonstrated in Section S.1 (Supporting Information). The thermal behavior is investigated in Figure 2a. The degradation temperature T_d is determined via the derivative of the weight loss versus temperature as shown in the left graph. The temperature at the maximum of the peak is reported as the degradation temperature in Table 1 which is for all composites in the range of 360 to 370 °C. It is apparent that the degradation temperature of all composite materials is nearly identical. The second heating cycle in the DSC test is shown in

© 2025 The Author(s). Advanced Functional Materials published by Wiley-VCH GmbH

16163028, 0, Downloaded from https://advanced.onlinelibrary.wiley.com/doi/10.1002/adfm.202512713 by Ku Leuven, Wiley Online Library on [23/09/2025]. See the Terms and Conditions (https://onlinelibrary.wiley.com/terms-and-conditions) on Wiley Online Library for rules of use; OA articles are governed by the applicable Creative Commons License

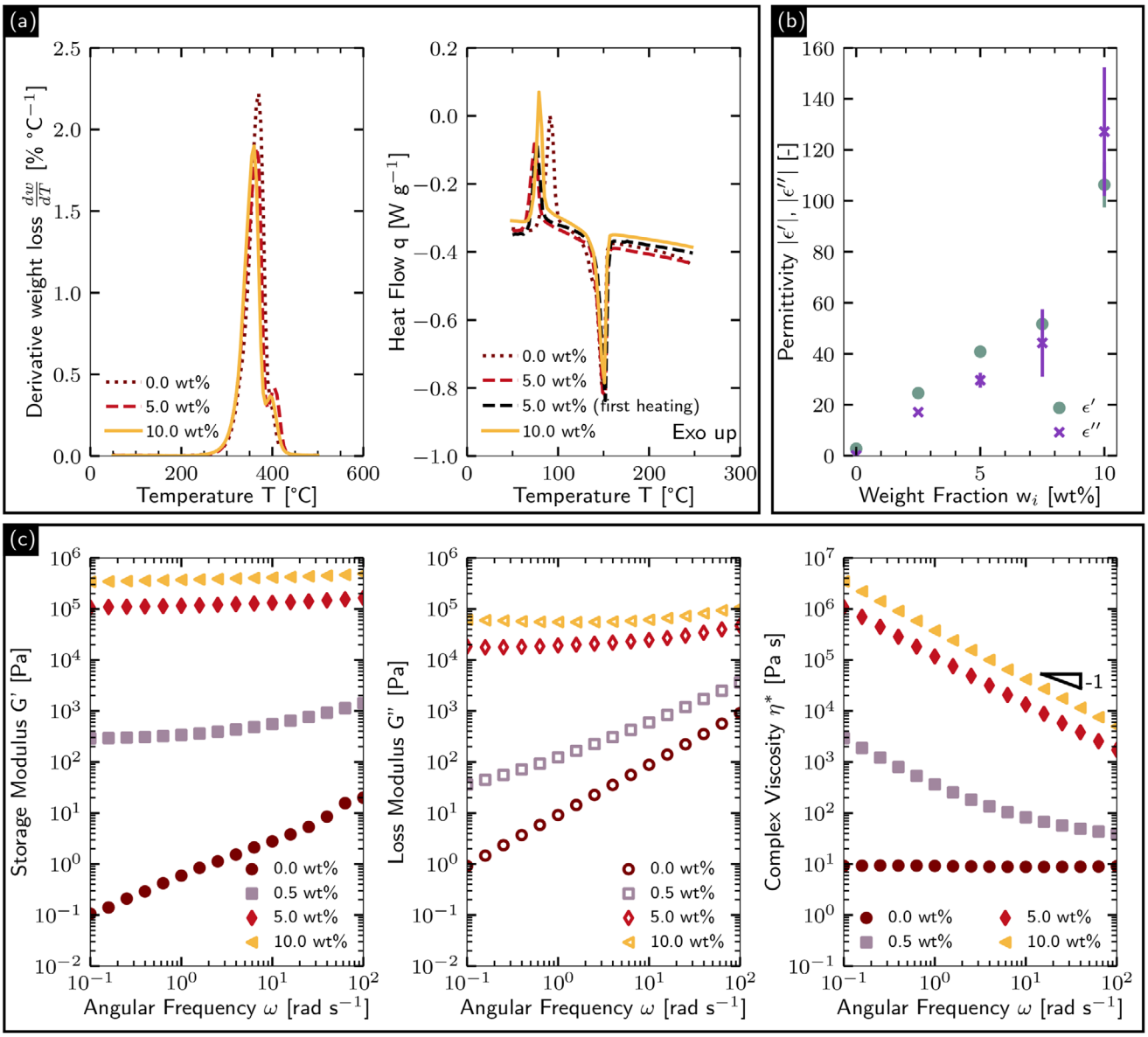


Figure 2. Material characterization of MWCNT/PLA nanocomposites. a) Thermal analysis of 0.0, 5.0, and 10.0 wt% composites to determine the degradation temperature (left) and the melting temperature (second heating run in DSC unless indicated otherwise) (right). b) Dielectric permittivity at 10 GHz as a function of the loading of the composites determined via the NRW method, the error bars indicate the standard deviation on the measurements. c) Rheological analysis at 190°C showing the storage modulus (left), loss modulus (middle) and complex viscosity (right) for 0.0, 0.5, 5.0, and 10.0 wt% composites.

the right graph of Figure 2a. Two distinctive peaks can be observed. The first one is an exothermic signal representing cold crystallization in the PLA matrix and the second is the endothermic signal determining the melting temperature of the material at the maximum of the peak. For the three composites shown, the melting temperature overlaps very well and is ≈150°C as reported in Table 1. The cold crystallization of the matrix occurs ≈70 °C at a heating rate of 10°C min^{-1}. Since the filament is only briefly in the melt state and this cold crystallization temperature is well above the temperature of the build plate to which the printed filament is quickly cooled after printing, no effect of this phenomenon is expected in the final printed material. However, the final printed part shows some crystallinity. The black dashed line in this graph represents the first heating cycle of the 5 wt% composite after printing. The difference in height between the cold crystallization peak and the melting peak indicates that some crystals are already present in the printed material. Figure S.1 (Supporting Information) shows the repeatability of the TGA analysis and the DSC measurements. Since the curves in Figure 2a overlap, the individual measurements are also shown in Figure S.2 (Supporting Information).

The complex dielectric permittivity, determined via the Nicolson-Ross-Weir method at 10 GHz,[30] of 1 mm uniform composite blocks produced by FDM is shown in Figure 2b. The

© 2025 The Author(s). Advanced Functional Materials published by Wiley-VCH GmbH

16163028, 0, Downloaded from https://advanced.onlinelibrary.wiley.com/doi/10.1002/adfm.202512713 by Ku Leuven, Wiley Online Library on [23/09/2025]. See the Terms and Conditions (https://onlinelibrary.wiley.com/terms-and-conditions) on Wiley Online Library for rules of use; OA articles are governed by the applicable Creative Commons License

real and imaginary part of the dielectric permittivity increase with the MWCNT loading indicating increasing polarization losses in the material. Error bars are shown on this figure to indicate the variation especially for densely loaded composites. Small variations in the manufacturing process can lead to substantial differences in the final EM properties due to differences in the total amount of filler in the structure, as well as filler dispersion and orientation. In this work, all composites are FDM printed with the same printing conditions (e.g. printing speed, infill percentage, layer height, nozzle diameter,...) to minimize variability. The dielectric permittivity as a function of frequency for these composites is shown in Figures S.3– S.7 (Supporting Information). The average rheological results of a frequency sweep at the selected print temperature of 190 °C are shown in Figure 2c for 0.0, 0.5, 5.0, and 10.0 wt% MWCNT nanocomposites. The left and middle panel show the storage and the loss modulus respectively and the right panel gives the complex viscosity. For the pure polymer, the loss modulus G'' is always higher than the storage modulus G'. The PLA material is liquid at the printing temperature and exhibits a Newtonian viscosity. The composite with 0.5 wt% MWCNT loading shows that the low frequency slope of G' with frequency goes to zero while G' exceeds G'' for frequencies below 8.5 rad s^{-1}, indicating that a percolated MWCNT network is present.[38] For the higher loadings, G' is always higher than G'' and the material behaves more solid-like. The repeatability of the rheological measurements is shown in Figure S.8 (Supporting Information) for the 5 wt% composite. Using the Cox-Merz rule, the complex viscosity η^* can be used to draw conclusions on the shear viscosity η.[39] The complex viscosity of the different nanocomposites is much higher than for the pure polymer and shows a slope of ≈–1 on a log–log plot indicating that the behavior in the probed shear rate range is fully dominated by the yield stress. Consequently, the material can only flow when a stress above the yield stress is applied. The yield stresses determined by this test range from 3 Pa for the 0.5 wt% composite to 3500 Pa for the highest loading of MWCNTs.

4.2. Learning the Electromagnetic Properties of PLA/MWCNT Nanocomposites

The addition of MWCNTs in the polymer matrix only changes the dielectric permittivity of the composite because these are highly conductive particles and can interact with the electric field of the EM wave, but exhibit no magnetic response. Therefore, the material is non-magnetic, i.e., the complex relative permeability $\mu(\boldsymbol{w}_i)$ is equal to one. For isotropic EMI shields $S_{11} = S_{22}$ and $S_{21} = S_{12}$ and the reference side can be either port of the vector network analyzer (VNA). However, this does not hold for asymmetric shields, like multilayered stacks. The front side of the stacks as we report them is always placed toward port 1. However, taking port 2 of the VNA as a reference, data for the inverse stack is obtained which is also useful as training data for the model. This way, the amount of training data is doubled without making extra stacks.

We explored three primary function classes to model the relationship between filler composition and the material's permittivity: linear, quadratic, and piecewise quadratic functions. The training dataset, presented in Tables S.1– S.3 in Section S.3 (Supporting Information), consists of 43 manufactured stacks of random layer order, 32 uniform shields of 2 mm thickness and 30 uniform shields of 4 mm thickness, so that $S = 105$. Upon solving learning problem in Equation (7) for different function classes, we obtained a training error (quantified by the corresponding value of Equation (7)) of 0.084 for linear functions, 0.076 for quadratic functions and 0.074 for piecewise quadratic functions. This suggests that the additional complexity introduced by the piecewise quadratic functions does not provide a substantial improvement over the quadratic model. Quadratic functions seem sufficient to accurately capture the relationship between filler composition and permittivity in these multilayer stacks. The resulting permittivity function is given by:

$$\epsilon(\boldsymbol{w}_i) = 3.438 + 9.973\boldsymbol{w}_i + 5.448\boldsymbol{w}_i^2 - j(0.133 + 15.413\boldsymbol{w}_i - 0.383\boldsymbol{w}_i^2) \quad (10)$$

which is visualized in **Figure 3**. Notably, it reveals a quadratic dependence of the real part of the permittivity function on the filler composition, while the dependence of the imaginary part is nearly linear. A large discrepancy between the results from the NRW analysis shown in Figure 2b and the trained function is apparent, mostly for the real part of ϵ. Because the model is trained on different orders of layers, it learns the effective permittivity of different concentrations inside these types of stacks while also taking variations in the filament loading, crystallinity in the layers and other aspects the manufacturing process might introduce into account. Moreover it compensates for the fact that the model assumes infinite layers in the direction perpendicular to the traveling direction of the wave, whereas experimentation was done in a waveguide.

4.3. Obtaining the Optimal Order for Layered EMI Shields

Intuitively, one would expect the EM wave to maximally enter into the body of the shield by closely matching the impedance of air at the incoming side of the shield. This corresponds to taking the first layer of the stack as the pure polymer and gradually increasing the loading throughout the shield to introduce energy dissipation by enhanced dielectric losses. The impedance step from each layer to the following should be small to allow most of the wave to be dissipated in higher filled areas of the shield while only a small amount is internally reflected toward previous layers.[19,20] Two types of these intuitive stacks are manufactured and tested, one wherein the loading increases linearly throughout the shield and one in which an exponential loading sequence is used. The order of the layers is respectively [0.0, 0.0, 2.5, 2.5, 5.0, 5.0, 7.5, 7.5, 10.0, 10.0] and [0.0, 0.5, 0.5, 1.0, 1.0, 2.5, 3.5, 5.0, 8.5, 10.0]. Both stacks are manufactured in triplet, tested and also used in the training of the model.

The trained permittivity function is used to calculate the order of loadings in a 10 layer stack which maximally absorbs EM energy. The choice for 10 layers in a 4 mm thick stack is twofold. On the one hand, 10 layers assure that the calculations can be executed in a decent time while still allowing the model to vary the composition in each layer when calculating the best discrete solution. On the other hand, these 10 layers per stack lead to a layer height of 0.4 mm which corresponds

© 2025 The Author(s). Advanced Functional Materials published by Wiley-VCH GmbH

16163028, 0, Downloaded from https://advanced.onlinelibrary.wiley.com/doi/10.1002/adfm.202512713 by Ku Leuven, Wiley Online Library on [23/09/2025]. See the Terms and Conditions (https://onlinelibrary.wiley.com/terms-and-conditions) on Wiley Online Library for rules of use; OA articles are governed by the applicable Creative Commons License

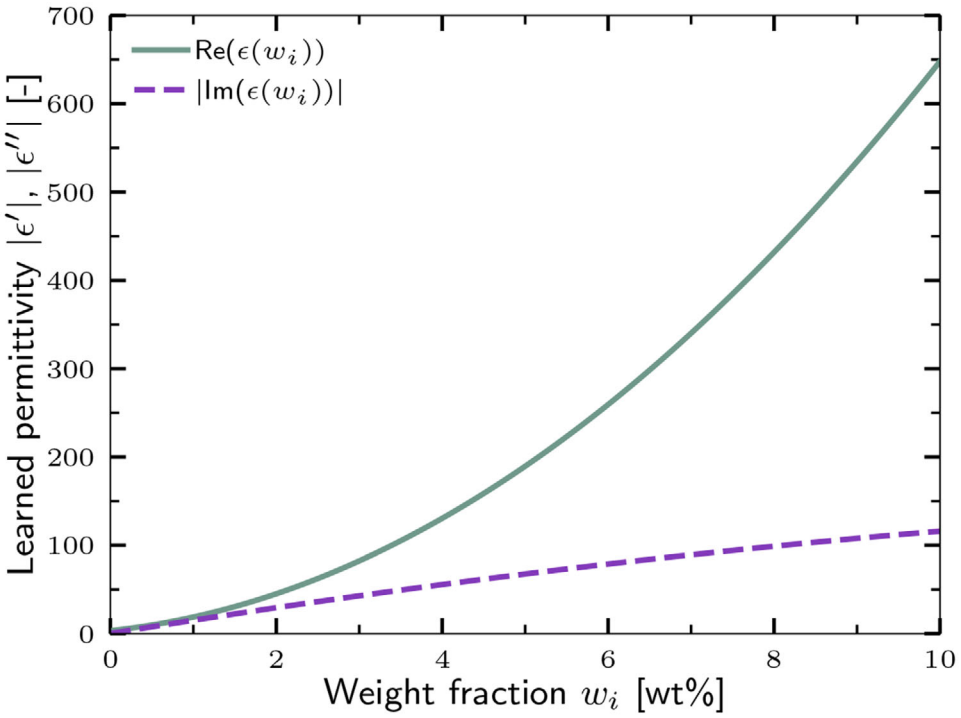


Figure 3. The learned permittivity function based on measurement results for 105 stacks.

to 2 printed layers of 0.2 mm, the standard resolution of FDM printers. A certain minimal shielding effectiveness is demanded and the frequency range over which the algorithm optimizes can be chosen. First an initial guess of the loading in each of the 10 layers is provided to the algorithm, from which it starts to change the loading of each layer by calculating the SE and the A/R until it cannot find a better solution. In **Table 2** the results of the optimization are shown for a minimal SE of 25, 30, 35, and 40 dB when optimizing over the entire X-band or at 8 GHz.

When taking a look at the predicted layer orders, they differ in a very important aspect from the proposed intuitive stacks, namely the first layer. There is no prediction where the first layer has a zero MWCNT loading, however, zero loadings are present in almost every stack and can occupy as much as half of the layers. The predictions for 25 and 30 dB follow the same trend, namely the wave encounters first a layer with a low loading, after which some layers with no or almost no loading are present and the stack ends with a number of highly filled layers. This type of ordering could be compared to a sandwich structure, which is already tested frequently in the literature.[21,40,41] However, note that our solution is not a symmetrical shield like most sandwich structures in literature and that the traveling distances for the EM wave in the stack do not correspond to $\lambda/2$ in the X-band, with λ being the wavelength of the EM wave. This emphasizes that absorption dominated EMI shields benefit from asymmetry in composition throughout the shield, as proposed by Zhou.[7] However, the solutions for a higher shielding effectiveness seem much more randomly ordered with an alteration of high and low filler loading.

Table 2. Predictions of the optimal layer order for different shielding targets. The first two columns indicate the targeted shielding response and the third column the optimal layer order for each case. The fourth column reports the average loading of the predicted stack. The last three columns give the predicted minimal shielding effectiveness, predicted minimal A/R and maximal A/R respectively.

Target		Prediction				
SE [dB]	f [GHz]	Optimal 10 layer order w [wt%]	w_{avg} [wt%]	$\min_{f\in\mathcal{V}}\{SE^f_{model}\}$ [dB]	$\min_{f\in\mathcal{V}}\{A^f_{model}/R^f_{model}\}$ [-]	$\max_{f\in\mathcal{V}}\{A^f_{model}/R^f_{model}\}$ [-]
25	8	[1.0, 1.0, 0.0, 0.0, 0.0, 0.0, 10.0, 10.0, 0.0, 10.0]	3.2	25.6	2.2	5.4
25	8-12	[1.0, 0.0, 0.5, 0.0, 0.5, 0.0, 10.0, 8.5, 0.0, 10.0]	3.1	25.1	4.1	8.7
30	8	[2.5, 0.0, 0.0, 0.0, 0.0, 10.0, 6.0, 0.0, 0.0, 10.0]	2.9	30.6	1.0	3.9
30	8-12	[1.0, 1.0, 0.0, 0.0, 6.0, 10.0, 2.5, 0.5, 0.0, 10.0]	3.1	30.1	2.0	3.2
35	8	[5.0, 0.0, 7.5, 10.0, 0.0, 6.0, 10.0, 0.0, 0.0, 10.0]	4.9	35.0	0.4	1.0
35	8-12	[3.5, 0.5, 10.0, 8.5, 0.5, 5.0, 10.0, 0.5, 0.5, 10.0]	4.9	35.0	0.8	1.0
40	8-12	[8.5, 3.5, 7.5, 10.0, 0.5, 5.0, 10.0, 0.5, 0.0, 10.0]	5.6	40.0	0.2	0.2

© 2025 The Author(s). Advanced Functional Materials published by Wiley-VCH GmbH

16163028, 0, Downloaded from https://advanced.onlinelibrary.wiley.com/doi/10.1002/adfm.202512713 by Ku Leuven, Wiley Online Library on [23/09/2025]. See the Terms and Conditions (https://onlinelibrary.wiley.com/terms-and-conditions) on Wiley Online Library for rules of use; OA articles are governed by the applicable Creative Commons License

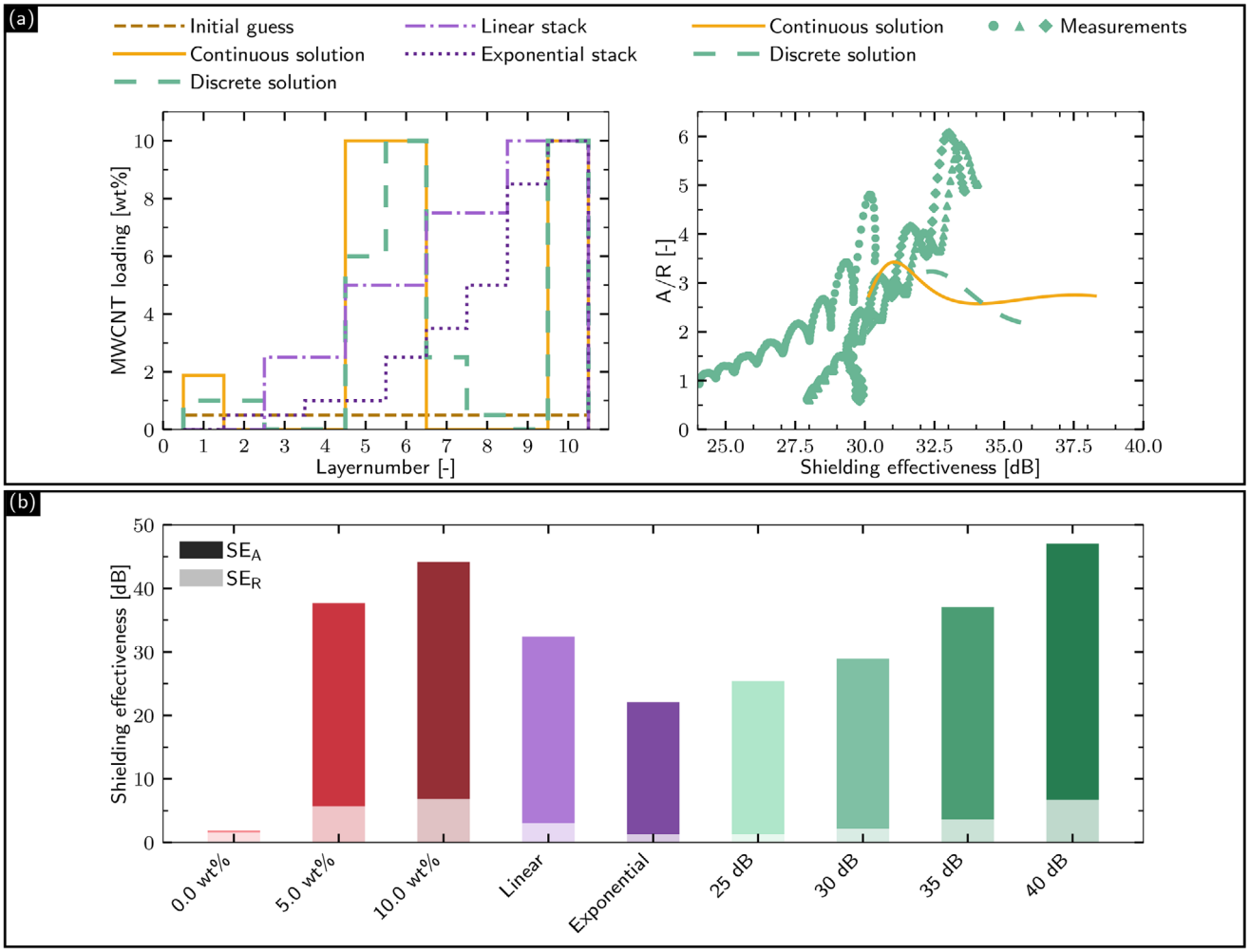


Figure 4. a) Algorithm prediction and measurements of the optimal stack for 30 dB shielding. (left) Predicted filler distribution with the highest absorption for 30 dB of shielding effectiveness and the linear and exponential loading profiles. (right) Predicted A/R, SE and measurement data for three different experimental realizations of the stack optimized for 30 dB shielding. b) Measured SE_A and SE_R in the X-band for uniform shields, intuitive stacks and for shields optimized for 25, 30, 35, and 40 dB shielding.

The other columns in Table 2 give more information about the predictions. The average loading of the whole stack is given by w_{avg}. It is apparent that for an optimal absorption, no more filler content is required for 30 dB than for 25 dB, ≈3 wt%, only the distribution of the fillers throughout the shield seems to play a role. The average filler content in the stack increases to 5 wt% and almost to 6 wt% when aiming for 35 or 40 dB of total shielding respectively. The last three columns give the predicted minimal SE, the minimal and the maximal predicted A/R for the 8–12 GHz range respectively. When the demanded SE increases, the average filler loading increases with it, and the obtainable A/R goes down as more filler means more reflection.[8]

Figure 4a illustrates the process of the prediction algorithm starting with the prediction of the MWCNT loading of each of the 10 layers for at least 30 dB of shielding in the X-band and the validation of the layered shield via measurements of the manufactured stacks. Moreover, the shielding effectiveness by absorption and reflection, SE_A and SE_R respectively, of uniform blocks, the intuitive and the optimized stacks for 25, 30, 35, and 40 dB are shown in Figure 4b. The left panel in Figure 4a illustrates the prediction of the most optimal layering of a 4 mm stack. Starting from the initial guess, illustrated by the dashed line, our optimization methodology first finds an optimal stacking by solving optimization problem in Equation (8) for the continuous interval $\mathcal{W} = [0, 10]$ using the basin-hopping algorithm, which is called the continuous solution and is visualized by the yellow line. In a second step, it iterates through all available loadings $\mathcal{W}$ as defined in Equation (9) to decide which available loadings are best to use in each layer and it generates the discrete solution, depicted as the green dashed line. To do this, the algorithm takes the $\ell = 4$ available concentrations nearest to the continuous solution at each layer and calculates the stack's performance for all resulting $4^{10} = 1048576$ stacks (see Section 3.2). The stack which performs best (having the highest A/R and sufficient shielding as in Equation (8)) is referred to as the discrete solution and is manufactured as described in Section 6.3 Additive Manufacturing of PLA/MWCNT Nanocomposite EMI Shields. For reference, the

© 2025 The Author(s). Advanced Functional Materials published by Wiley-VCH GmbH

16163028, 0, Downloaded from https://advanced.onlinelibrary.wiley.com/doi/10.1002/adfm.202512713 by Ku Leuven, Wiley Online Library on [23/09/2025]. See the Terms and Conditions (https://onlinelibrary.wiley.com/terms-and-conditions) on Wiley Online Library for rules of use; OA articles are governed by the applicable Creative Commons License

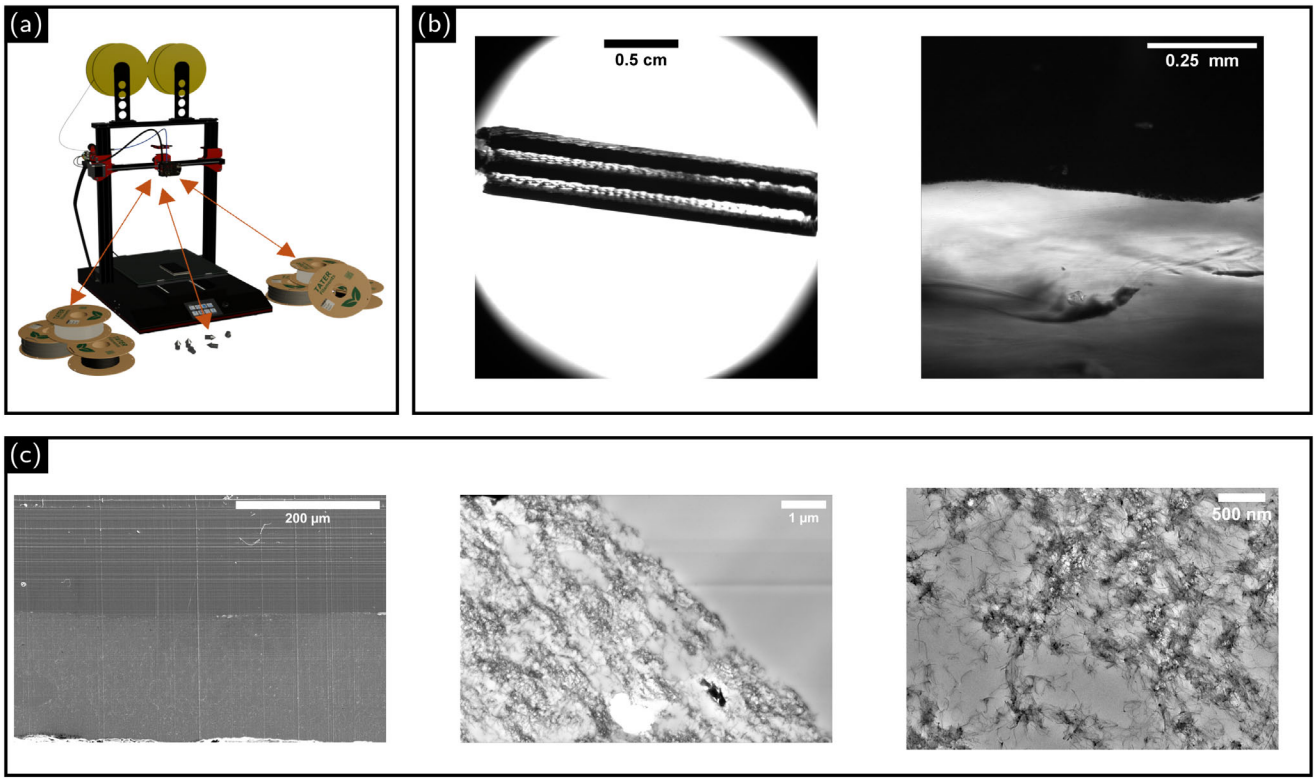


Figure 5. a) Visualization of the multi-filament and multi-nozzle printing technique. b) Optical images of a printed alternating multilayer. (left) A five layer alternating stack produced by fused deposition modeling and (right) microscopic view of the interface between a transparent and a black layer. c) (left) SEM image of the interphase between a pristine PLA and a 10 wt% MWCNT layer in a printed stack. (middle) STEM image of the interphase between a pristine PLA and a 10 wt% MWCNT layer in a printed stack. (right) TEM image of the MWCNT dispersion in the printing plane for a 10 wt% composite.

loading profiles of linear and exponential stacks are also depicted in Figure 4a.

The right graph in Figure 4a shows the predicted behavior of the continuous and discrete solutions as A/R versus SE from 8 GHz on the left to 12 GHz on the right side of the curve. These predictions show that the desired total shielding effectiveness is obtained over the whole X-band and that the green index is always greater than one, indicating that our resulting EMI shields are indeed absorption-dominant as desired.[7] However, when looking at the measurement data of three productions of an optimized stack, a discrepancy between prediction and reality is observed, as well as some variability between different productions of the same stack. The required shielding effectiveness of 30 dB is not reached throughout the complete X-band and the A/R values span a greater range than predicted, reaching worse and better values than the model. This variability can be attributed to the unavoidable variation in the additive manufacturing process in which filament diameter, filler distribution, orientation and composition are not always uniform, leading to over and underextrusion of functional filler at different locations throughout the shield. Moreover, the height setting upon switching filaments is not always perfect.

The printing technique is visualized in **Figure** 5a. This figure shows a commercial FDM printer with multiple filament spools, indicating the different used nanocomposites and multiple nozzles, with a different one being used for each loading. Figure 5b shows optical microscopy pictures of the cross section of a printed alternating A-B multilayer stack. This stack is printed in the same way as the optimal layered stack but now each time 4 layers of 0.2 mm are printed to obtain 5 alternating black and white zones of 0.8 mm thick, to facilitate optical imaging. The samples are cut and polished before observation under the microscope. The left panel is a picture taken by a stereomicroscope. It clearly shows that light is able to travel through the transparent pure PLA layers. The darker patterns in the transparent layers show the adjacently printed strands of MWCNT-containing filament of the zigzag infill where light scatters. The picture on the right in Figure 5b is a close up of the interface between a transparent and a black layer taken under a regular microscope in transmission mode. A clean and slightly wavy interface between the two zones can be observed indicating that no porosity is present between the layers. The waviness of the surface is not directly included in the model, but is also present in the training dataset. Moreover, mismatches in prediction and measurement might be explained by microstructural differences induced by the filament making or printing process which cannot be observed via microscopy. It should also be kept in mind that the model is based on the free space wave response. Zooming in further, the left panel in Figure 5c shows a scanning electron microscopy (SEM) image of the interface between two layers of a printed stack. The SEM image shows that the interface is smooth and that no porosity is present. The middle panel in Figure 5c shows

© 2025 The Author(s). Advanced Functional Materials published by Wiley-VCH GmbH

16163028, 0, Downloaded from https://advanced.onlinelibrary.wiley.com/doi/10.1002/adfm.202512713 by Ku Leuven, Wiley Online Library on [23/09/2025]. See the Terms and Conditions (https://onlinelibrary.wiley.com/terms-and-conditions) on Wiley Online Library for rules of use; OA articles are governed by the applicable Creative Commons License

a scanning transmission electron microscopy (STEM) image of the interface between two layers of a printed stack. The STEM image shows there is a clear and distinct boundary between the MWCNT-containing and printine PLA layers. The right panel in Figure 5c shows a transmission electron microscopy (TEM) image of the MWCNTs in the PLA matrix. The TEM image shows that the MWCNTs are well distributed throughout the PLA matrix and form a network consisting of MWCNT bundles connected by single MWCNTs. STEM and TEM images at different magnifications are shown in Section S.4 (Supporting Information).

Figure 4b allows to assess the performance of the optimized shields compared to uniform blocks and intuitive stacks. In this figure, the average SE_A and SE_R in the X-band of uniform shields of 0.0, 5.0, and 10.0 wt% can be observed together with the results for intuitive stacks with linear and exponential profiles of the loading. It is hard to determine the dominant shielding mechanism from these figures since only the shielding effectivenesses are shown, but these are more straightforward to compare with already existing literature. It is worth to mention here that a higher SE_A than SE_R does not mean that the shielding is dominated by absorption. This is an obstinate misconception in many published papers as thoroughly explained by Peng et al.[29] Briefly, SE_A indicates the effectiveness of the absorption mechanism on the fraction of the energy which is not reflected. Only the power coefficients A, R and T can indicate the dominant shielding mechanism. Note that A and R can be calculated from SE_A and SE_R as explained in Section S.2 (Supporting Information). Notably, only when SE_R is lower than 3 dB, the shielding is dominated by absorption.[6] It is apparent that uniform shields with a higher MWCNT loading exhibit a better total shielding (higher SE_A and SE_R) but are also more reflection dominated. Because reflection takes place before absorption, the higher the SE_R, the more energy is already reflected before it can be absorbed. Looking at the intuitive stacks, it can be seen that they show a lower SE_R compared to the 5.0 and 10.0 wt% shields, meaning more energy is able to penetrate into the shield. Especially the comparison between the linear stack and the 5.0 wt% block is relevant because these have the same equivalent loading but a different spatial distribution of the filler. These results clearly demonstrate that a rearrangement of filler in the shield can significantly alter its overall shielding performance and reduce the reflection contribution. Adding the SE_A and SE_R, the total SE is obtained,[29] which goes as high as 45 dB for a 10.0 wt% block and approaches 30 dB in the case of a linear stack. The four last bars in Figure 4b show the shielding efficiencies for the optimized stacks, averaged over the X-band and with minimum shielding requirements of 25, 30, 35, and 40 dB. No significant frequency dependence was observed for all these measurements. It is no surprise that for a constant thickness, more reflection is needed to meet higher SE requirements. What stands out is that the optimized stacks perform equally or better than the uniform shields in terms of total shielding, but always with a lower filler loading and a lower contribution of reflection. One example is the 40 dB optimized stack. When looking back in Table 2, one can see that the equivalent loading of this stack is only 5.6 wt%, yet it outperforms the uniform 10.0 wt% shield in total SE with a lower SE_R and a higher SE_A, saving filler and decreasing reflection. In Section 4.4 a more profound look into the green index of these optimally layered shields is provided.

4.4. Shielding Effectiveness and Green Index of Optimally Layered EMI Shields

Figure 6 summarizes the shielding performance of the intuitive and predicted optimal stacks discussed above. Each stack is produced in triplet and the averages of the shielding effectiveness SE and the green index A/R are calculated and presented on the plot, as well as a selection of data from the literature on comparable EMI shields, represented by the red crosses. To give an overview of the current state of the art, these data comprise EMI shields produced by FDM and tested in the X-band for various thicknesses, conductive fillers and material compositions. Since often only shielding effectiveness values are reported, a calculation toward the green index is performed as explained in Section S.2 (Supporting Information). The target performance for most applications is a shielding effectiveness above 25 dB which is ideally reached with a green index of at least one, meaning that the fraction of energy which is absorbed is at least equal to the reflected fraction.

The data for shields with linear and exponential loading profiles are depicted in light and dark purple, respectively, and the averages of the three samples at 8, 10, and 12 GHz are correspondingly shown by circles, squares and diamonds. Since most stacks have an equivalent loading between 3 and 6 wt%, the results of uniform shields of 4 mm thickness and loadings of 3.5 and 5 wt% are also shown as a reference in red. The data for the linear loading profile can directly be compared to that of the 5 wt% sample as both shields have an identical total amount of filler. However, by spatially reordering the filler in the shield and attempting a better impedance matching at the incoming side, the reflection goes down, but unfortunately, so does the shielding effectiveness by more than 5 dB. Furthermore, the green index rises above one for frequencies higher than 10 GHz which is an indication that not only the amount of filler in the shield plays a role, but its distribution is also important when aiming for absorption dominant shields. A trade-off seems present between SE and A/R for multilayer EMI shields when following intuition.[8] The equivalent loading of the stack with exponential loading profile is 3.2 wt%. Similar conclusions with respect to the uniform 3.5 wt% shield can be drawn. The total shielding effectiveness goes down while the absorption increases significantly. In this case a green index well above one is reached for the entire X-band while almost reaching 25 dB of shielding at 12 GHz.

Data for the stacks with layer sequences optimized for the entire X-band and 25, 30, 35, and 40 dB shielding effectiveness are shown in increasingly darker green symbols. Individual measurements of the three different samples of each optimized stack are shown in Section S.5 (Supporting Information). Assessing a general trend, the green index decreases as the shielding effectiveness for which the optimization is performed increases, indicating again the trade-off between SE and A/R. This can intuitively be understood by physical arguments since more shielding requires more filler which inevitably leads to more reflection due to a larger impedance mismatch between the shield and air. We point out that each of the predicted stacks meets its intended shielding requirement and that exceptionally high A/R ratios are obtained in the case of 25, 30, and 35 dB of shielding effectiveness. Each stack outperforms current findings in literature exhibiting green indices approaching 100 at an SE of 25 dB, which

© 2025 The Author(s). Advanced Functional Materials published by Wiley-VCH GmbH

16163028, 0, Downloaded from https://advanced.onlinelibrary.wiley.com/doi/10.1002/adfm.202512713 by Ku Leuven, Wiley Online Library on [23/09/2025]. See the Terms and Conditions (https://onlinelibrary.wiley.com/terms-and-conditions) on Wiley Online Library for rules of use; OA articles are governed by the applicable Creative Commons License

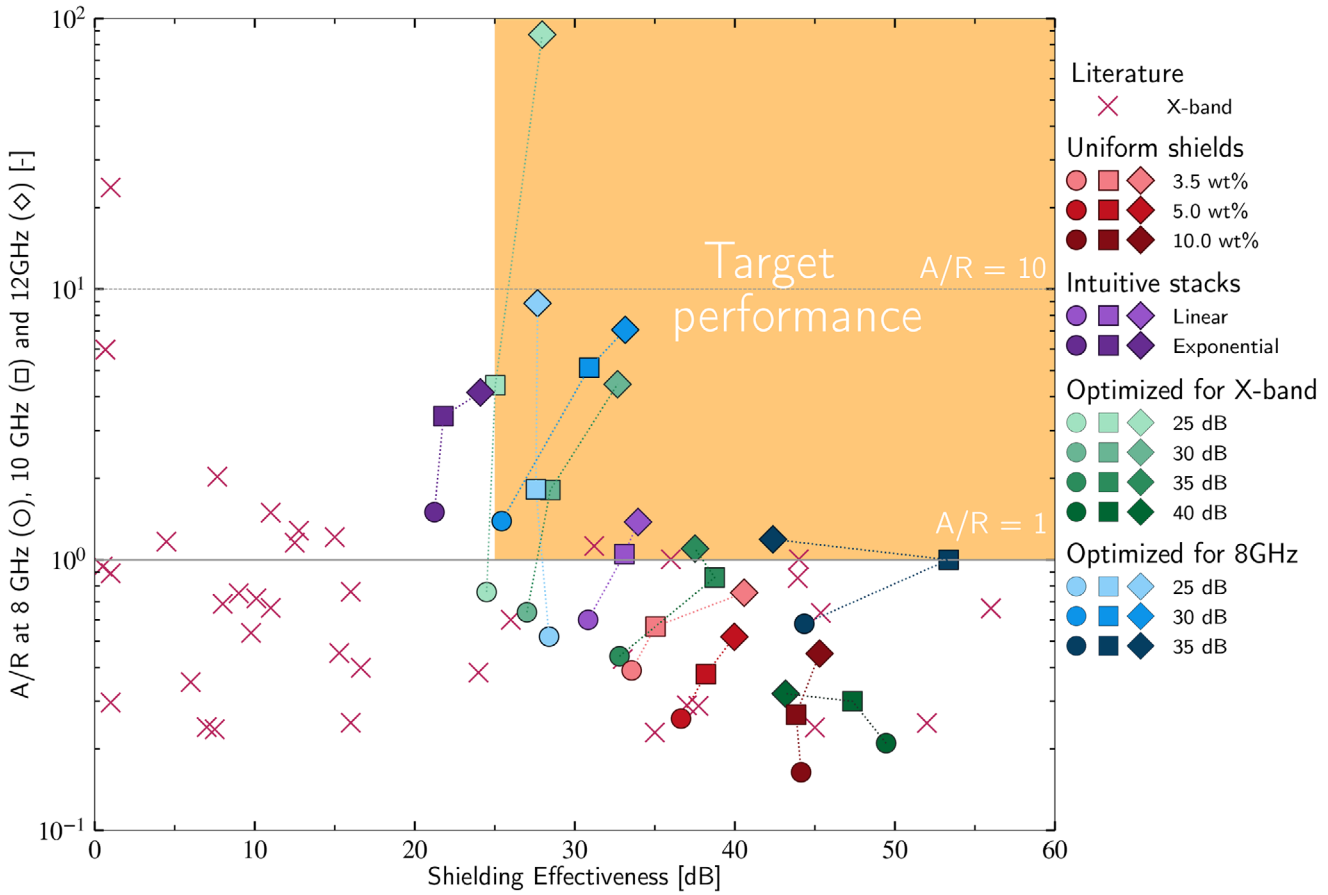


Figure 6. Shielding performance of optimized layered shields produced by additive manufacturing. The target performance is indicated as a minimal shielding effectiveness of 25 dB and a green index of at least one. The red crosses depict values of comparable EMI shields in the X-band found in literature.[42–49] Uniform shields with loadings of 3.5, 5, and 10 wt% are visualized in red. The circles, squares and diamonds represent averaged data of measurements at 8, 10, and 12 GHz respectively. Light and dark purple markers indicate corresponding measurements of the linear and exponential stacks. Green markers illustrate stacks optimized over the entire X-band and are darker for higher required shielding effectiveness. Blue markers indicate stacks optimized for 8 GHz and are darker for higher desired shielding effectiveness.

means that there is almost no reflection and this is to the best of our knowledge unseen for multilayer shields produced by additive manufacturing.

A possible explanation can be found by looking at simulations of the EM wave traveling through this stack as shown in **Figure** 7a. In these simulations, capturing the material behavior in a waveguide, the material properties measured by the NRW method and reported in Figure 2b are used as those of the learned permittivity model deviate significantly from the true material properties at high loadings. A more detailed procedure is described in Section Simulation of EMI shielding by multilayer structures. The incoming wave penetrates the stack from the top side and is almost undisturbed by the first 6 layers in which the filler loading is low. When reaching layer 7, which contains 10 wt% of MWCNT, the wave is largely reflected and destructively interferes here with the incoming waves, explaining the very low general reflection of this stack. Moreover, looking at the effective relative impedance of the stack as depicted in Figure 7b, it closely matches with the impedance of air, allowing most of the EM energy to enter the material of the shield. This mechanism is already proposed by other researchers in other types of EMI shields.[50,51] However, a small part of the wave is still able to pass through layer 7 whereafter energy can be dissipated by the last layers of the stack or can still be reflected back toward the front of the shield or can travel through the whole shield resulting in transmission. Taking a closer look at the Schmidt chart, which shows the complex impedance of the stack as a function of frequency from 8 GHz at the leftmost point to 12 GHz, in the left graph of Figure 7b, the explanation for this extreme high green index can be confirmed. Approaching 12 GHz, the characteristic impedance of the stack, relative to air, approaches 1 on the chart, which means perfect impedance matching with the surrounding medium, hence no net reflection. The left graph in Figure 7c shows a comparison of the simulated shielding of this stack and the measurements. This graph also supports the previous findings, showing that SE_R approaches 0 going to 12 GHz. We again notice the almost perfect agreement between simulated and measured data in this plot.

Figure 7 also shows the comparison between simulations and measurement data for the intuitive stack with a linear loading profile in the rightmost panels. The incoming wave attenuates earlier in this stack as compared to the stack with layer sequence

© 2025 The Author(s). Advanced Functional Materials published by Wiley-VCH GmbH

16163028, 0, Downloaded from https://advanced.onlinelibrary.wiley.com/doi/10.1002/adfm.202512713 by Ku Leuven, Wiley Online Library on [23/09/2025]. See the Terms and Conditions (https://onlinelibrary.wiley.com/terms-and-conditions) on Wiley Online Library for rules of use; OA articles are governed by the applicable Creative Commons License

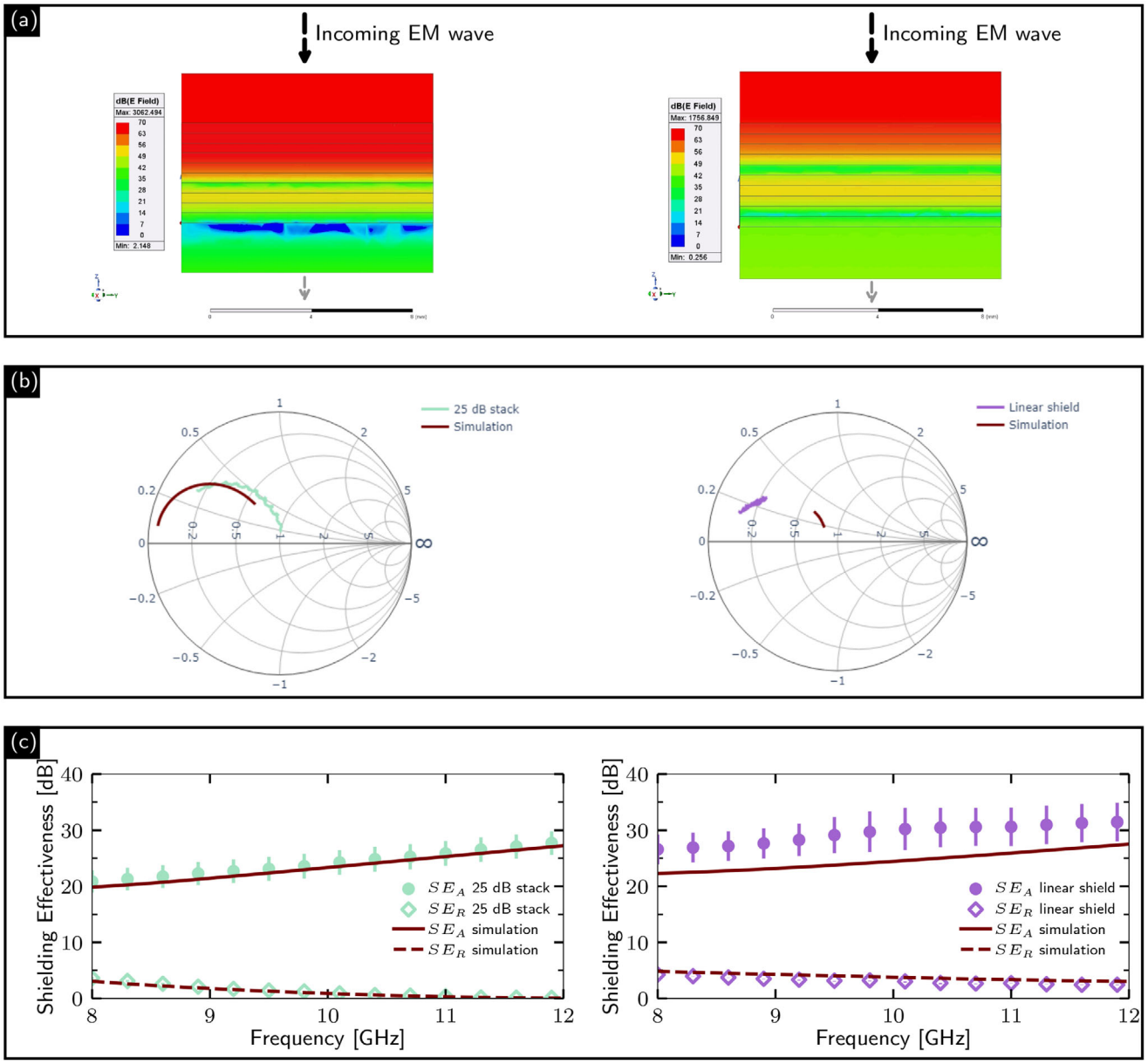


Figure 7. Comparison between simulated and measured shielding response for (left) the optimal layer order designed for 25 dB shielding across the X-band and (right) the intuitive stack with a linear loading profile. a) Simulations of an EM wave passing through the multilayer shields. b) The Smith charts showing the simulated and measured impedances of the shields. c) The simulated and measured shielding effectivenesses SE_A and SE_R.

optimized to maximize the A/R while reaching at least 25 dB of shielding. The simulation in Figure 7a reveals no significant attenuation in the first three layers, however once reaching layer 5 some reflection can be noticed comparable to what happens at layer 7 in the left panel of Figure 7a. Part of the wave's energy is reflected and finds its way back to the front of the shield while the rest can penetrate deeper and can be dissipated in the higher MWCNT loaded layers or can be transmitted at the rear side of the shield. When looking at Figure 7c, it can be observed that the simulation captures the reflection of the stacks very well. However, it underpredicts the impedance mismatch and the absorption efficiency of the shield. The trend of the predicted SE_A is similar to the measured trend, but a discrepancy of ≈5 dB is observed. Similar mismatches in model predictions and measurements are already observed in previous work on multilayer structures.[8]

Similar reasoning to explain the performance of the 25 dB stack can be used for the 30 dB stack. As already mentioned, increasing the shielding requirement leads to an increased total loading of the stack and a reduced green index. However, we want to point out that nonetheless, the predicted stacks meet these requirements for 35 and 40 dB while outperforming the heavier loaded uniform stacks in SE and green index. These findings and this methodology open a new door to the design of

© 2025 The Author(s). Advanced Functional Materials published by Wiley-VCH GmbH

16163028, 0, Downloaded from https://advanced.onlinelibrary.wiley.com/doi/10.1002/adfm.202512713 by Ku Leuven, Wiley Online Library on [23/09/2025]. See the Terms and Conditions (https://onlinelibrary.wiley.com/terms-and-conditions) on Wiley Online Library for rules of use; OA articles are governed by the applicable Creative Commons License

asymmetrical EMI shields, optimized for high absorption while saving in material use.

When looking at the frequency trend of the optimal ordered stacks (green symbols) in Figure 6, it appears as if at higher frequencies, outside the X-band, even higher A/R ratios could be acquired for these layered shields. Therefore, the model is also used to optimize 10 layer stacks only for 8 GHz instead of over the entire X-band to try to shift the optimal response into the measurement range. The resulting layer sequences can also be found in Table 2 and the measurement data are visualized as blue markers in Figure 6. The results for 35 dB (dark blue) immediately catch the eye because of their drastically improved SE for a comparable green index across the X-band. Obtaining even higher total shielding than a uniform shield of 10 wt% MWCNTs and a green index of approximately one is remarkable with only half the amount of filler. In general, these shields show the same trend as their counterparts, which are optimized over the entire X-band but perform slightly better overall.

Two main conclusions can be dawn from our work. First, we demonstrate a method to optimize the order of several layers in a nanocomposite EMI shield to promote absorption at the cost of reflection and with a reduced filler content by smartly distributing the filler throughout the shield. While the training of such a model might be cumbersome, the result is spectacular when looking at the overall performance and obtained green indices for these optimized shields. Our multilayer structures show the targeted high absorption dominated shielding. Second, a production method is established to obtain very clean interphase transitions between the layers of a stack by additive manufacturing to approach the theoretical solutions as well as possible, which is supported by the results of the simulations.

Note that our approach is not limited to additive manufacturing or EMI shielding applications. In fact, layered structures are employed in many different applications such as piezoelectric composites,[52] multilayer scintillators,[53] multilayer membranes[54] or modular steam electricity cogeneration systems,[55] to name only a few. Other commonly used manufacturing methods include for instance compression molding[56] and coating techniques.[57] By simply defining an objective function and gathering a sufficiently large training dataset, our methodology is applicable to a myriad of fields.

5. Conclusion

The main conclusion of this work is that highly effective and extremely absorption-dominated EMI shields can be manufactured using a layered approach, which can be conveniently done using multi-nozzle fused deposition modeling. By smartly distributing the filler content throughout the shield, one can trigger the absorption mechanism to dominate by impedance matching and consequently internal destructive interference much more than the reflection without the need of adding more fillers. Using PLA/MWCNT nanocomposite filaments as a base material for this purpose, we learned the permittivity function of the produced materials in a sample-efficient manner, using 105 samples. With this model, predictions were made for the most absorbing sequence for the case of 10 layers in a 4 mm stack. These ordered shields consist of non-intuitive orders, in contrast to A-B multilayers, linear gradient and sandwich structures, and prove to outperform their uniform equivalents, comparable shields in the literature and shields with a simple linear or exponential loading profile. Green indices well above 1 and ranging up to 100 are obtained for stacks which can also obtain a shielding effectiveness of up to 40 dB.

We want to point out two key findings of our research. The first is the ultra-high obtained green index of ≈100 for the 25 dB shielding stack. This means that there is virtually no reflection from the shield while only ≈0.1% of the incoming energy is able to transmit through the shield. Comparing this layered shield with a uniform shield of comparable equal average loading, the shielding effectiveness is lower, but the absorption is much higher. Second, by redistributing 5 wt% of MWCNT in the shield as shown in the optimal case for 35 dB of shielding and 8 GHz as target frequency, extremely high shielding effectiveness is obtained, ranging to almost 55 dB which outperforms even a uniform shield with double this loading, while still reaching a green index ≈1. This indicates that the future focus should not be on achieving the highest possible filler loading in polymer materials for EMI shielding purposes, but rather on finding new ways to determine the best distribution of fillers throughout the shield to meet the requirements of the target application. All our observations strive to move the field of absorption-dominated EMI shielding forward. It is evident that asymmetric shields offer a substantial advantage over uniform ones, and that system identification and optimization techniques hold great potential for determining the optimal layer distribution in multilayer shields.

6. Experimental Section

Manufacturing of PLA Composite Filaments: Commercial polylactic acid (PLA) pellets (123-3D.nl, The Netherlands) for 3D printing filament preparation were pulverized into a powder in a rotor mill Pulverisette (Fritsch, Germany) at 13 000 rpm with a 1 mm sieve. As the functional filler, NC7000 (Nanocyl, Belgium) multiwalled carbon nanotubes (MWCNT), a type of filler which is often used for EMI shielding applications, were chosen for their high aspect ratio, general availability and high electrical conductivity. A plasticizer, polyethylene glycol 3350 (PEG) (Sigma Aldrich, Germany) was used to obtain non-brittle composite filaments. Powder mixtures of different filler compositions (0, 0.5, 1.0, 2.5, 3.5, 5.0, 6.0, 7.5, 8.5, 10.0, and 15.0 wt% MWCNT) were prepared with a PLA to PEG ratio of 7:1. The powder mixtures were sent through a Process 11 twin screw extruder (ThermoFischer, USA) with a die of 2 mm to produce filaments with a diameter ≈1.75 mm, which can be used on a commercial FDM printer. The Process 11 twin screw extruder was equipped with two mixing sections along the screws to ensure a homogeneous distribution of the filler in the PLA matrix.

Characterization of PLA/MWCNT Nanocomposites: Thermal characterization of the materials was carried out with a TGA Q500 (TA Instruments, USA) and a DSC Q2000 (TA Instruments, USA). To obtain the degradation temperature T_d, the samples were heated in the TGA from room temperature to 550 °C at a rate of 10 °C min^{-1} in air after which they were held isothermally for 10 min. T_d was determined as the temperature at which the maximum in the mass change occurs. All thermogravimetric tests were performed on samples of similar age to reduce the influence of any ageing effects on the composite material. The residue left at the end is a good estimate for the effective filler loading of the filament since only the filler particles should be left after total degradation. Furthermore, thermal stability at the printing temperature was tested by holding the samples isothermally at this temperature while monitoring the weight loss for 90 min.

Temperature ramps at 10 °C min^{-1} from 20 to 250 °C and back were performed in the DSC to obtain the melting temperature T_m of all composites. The samples undergo the thermal cycle twice where the first cycle

© 2025 The Author(s). Advanced Functional Materials published by Wiley-VCH GmbH

16163028, 0, Downloaded from https://advanced.onlinelibrary.wiley.com/doi/10.1002/adfm.202512713 by Ku Leuven, Wiley Online Library on [23/09/2025]. See the Terms and Conditions (https://onlinelibrary.wiley.com/terms-and-conditions) on Wiley Online Library for rules of use; OA articles are governed by the applicable Creative Commons License

was meant to erase all thermal history of the material and the second one was the measurement cycle. T_m was determined as the temperature at the maximum of the endothermic peak in the second run.

A frequency sweep at a strain of 1% was performed on an MCR501 rotational rheometer (Anton Paar, Austria) with a forced convection oven and 25 mm parallel plate geometry to obtain the complex viscosity η^* and shear moduli G' and G'' for each composition at the printing temperature of 190 °C under N_2 atmosphere. This strain was verified to be in the linear range for all composites.

For the EM characterization, the reflection and transmission responses, i.e., the S-parameters, from the 3D printed uniform shields and randomly ordered stacks (see Section Additive Manufacturing of PLA/MWCNT Nanocomposite EMI Shields) are obtained using a 2-port vector network analyzer (VNA) type ZNB (Rohde&Schwarz, Germany) for X-band measurements (8–12 GHz) with waveguide dimensions of 22.86 mm by 10.16 mm (WR90) and sample thicknesses of 2 and 4 mm. The obtained S-parameters were used for learning the composites' permittivity function as described in Section 3. Moreover, the Nicolson–Ross–Weir method[30] was applied on measurements of 1 mm thick uniform samples to obtain the complex permittivity of the pure composites as a comparison to the trained function. There can be an ambiguity in the obtained ϵ and μ values as different integer values of nt/λ result in the same response. The n parameter was chosen as such that the permeability of the measured materials was closest to 1 since no magnetic response was expected. Here, n was 0 for all samples of 1 mm thickness. The optimized ordered stacks, predicted by the model, were manufactured and measured in the same way and the shielding results were used to calculate the shielding effectiveness and the green index as described in Section 2. All measurements were performed on three different samples of which the average results are reported in this work.

Alternating transparent and MWCNT loaded layers were printed to asses the accuracy of the filament changing printing method, the layer adhesion and the shape of the interface after switching the filament and nozzle. This printing procedure is described in more detail in Section Additive Manufacturing of PLA/MWCNT Nanocomposite EMI Shields. The A-B multilayer structures were cut in half along the long edge and the long sides were first sanded and then polished to obtain smooth and flat surfaces. Two types of optical images are taken of the smooth faces. First a Hamamatsu C13440 camera (Hamamatsu, Japan) equipped with a x4 lens was aimed at the sample which was placed on an LED. This gives a view on all layers. Second, the sample was placed under a regular microscope (Olympus, Japan) in transmission mode. Using a x10 magnification, the interface between two layers was investigated in more detail.

Two types of printed samples were used to assess the distribution of the filler and the interphase quality. A rectangular sample made entirely of the 10 wt% MWCNT filament was used to study the MWCNT dispersion via TEM and a three layer sample consisting of two pure PLA layers and one top layer of the 10 wt% MWCNT composite was used to investigate the interphase via SEM and STEM. For Transmission Electron Microscopy (TEM) analysis as well as Scanning Transmission Electron Microscopy (STEM) ultrathin sections ≈50 nm in thickness were prepared at room temperature using a LEICA ULTRACUT UCT ultramicrotome (Leica, Germany) equipped with a diamond knife, ensuring minimal deformation and optimal electron transparency. In addition, the block face of the sample was trimmed and prepared for Scanning Electron Microscopy (SEM) imaging under similar ambient conditions. TEM imaging was conducted using a FEI TECNAI Osiris transmission electron microscope (FEI company, USA) operated at an accelerating voltage of 200 kV in bright field (BF-TEM). Complementary SEM and STEM analyses were performed using a FEI SEM TENEO system (FEI company, USA) equipped with integrated STEM detectors.

Additive Manufacturing of PLA/MWCNT Nanocomposite EMI Shields: Two types of 3D models were made using the Shapr3D modeling software (Shapr3D Zrt., Hungary). One is a circular disk of 25 mm in diameter to rheologically characterized the materials and the other one was a rectangular disk of dimensions 10.16 mm × 22.86 mm to fit a WR90 waveguide for the EM characterization. The models were sliced in Ultimaker Cura 5.7.2. (Ultimaker, The Netherlands) for printing on a Sermoon D1 3D printer (Creality, China). The original 3D printer extruder system was changed to a dual gear Sprite extruder (Creality, China) to ensure more uniform printing of the in-house made filaments. The printer modifications were based on a Thingiverse project.[58] Stainless steel nozzles of standard 0.4 mm diameter (RS Components, UK) were used to print all samples. The layer height was set to 0.2 mm and the infill density is 100% with a zigzag pattern. The print speed is set to 25 mm s^{-1} with a flow percentage ranging from 80 to 110% based on the measured diameter of the filament to compensate for larger or smaller than ideal diameters. The nozzle temperature and the build plate temperature are respectively 190 and 45 °C. Rectangular bars of uniform composition and thickness of 2 and 4 mm were manufactured in triplets for each concentration of filament, as well as circular disks of thickness 1 mm. Furthermore, randomly ordered shields were produced by mimicking a 10 nozzle printer (one nozzle for each concentration). To ensure a clean transition between layers of different filler concentration, the filament and nozzle are changed at each composition transition. Each shield was built from monolayer models of thickness 0.4 mm and offset by the height of the already printed part. This means that every material transition corresponds to starting a new print at the same location where the previously discussed parameters were adapted for the next filament. When multiple consecutive layers have the same composition, the model was scaled in the z-direction to print these layers without interruption. When a transition of composition occurs, the printer was stopped while the bed remains at the printing temperature. The nozzle of the previously printed filament was taken out, the channel was cleaned and the nozzle for the next filament was mounted. After this procedure, the hotend was heated to the printing temperature again, the next layer was sliced and the Z-offset setting was set to the corresponding height. This workflow assured that all layers were printed nicely on top of each other and that a clean transition between different compositions is obtained.

Simulation of EMI Shielding by Multilayer Structures: The comparing simulations were executed in Ansys Electronics 2024 R1 using the frequency-domain finite element method (FEM) with a driven modal solver. The first step was modeling ten layers of WR90 dimensions stacked on top of each other. Material properties were assigned to each layer as the real part of the permittivity and the dielectric loss tangent $\tan\delta = \epsilon'' \cdot \epsilon'^{-1}$. The permittivity values of each composite filament can be found in Section S.6 (Supporting Information). An enclosure was created around the layered structure, to capture the propagation of EM waves in a waveguide section. The outer walls were assigned with perfect electric conductor (PEC) conditions to replicate the conditions in the waveguide. Wave port excitation was assigned on both ends of the computation domain along the propagation direction with an integral line to establish the TE10 mode. Adaptive meshing was performed with a convergence criterion of $\Delta S = 0.001$, meaning the difference in S-parameters between successive adaptive passes being less than 0.001. The simulation was performed for a frequency range of 8–12 GHz with 201 sweep points.

Data processing and visualizations: All measurement data[59] was processed using in-house Python code (version 3.13.1) in VS Code (version 1.97.0). Figure 5a was adapted from Blenderkit (version 3.15.1) 3D printer and PLA filament spool models using Blender 4.4.0.

Supporting Information

Supporting Information is available from the Wiley Online Library or from the author.

Acknowledgements

The authors gratefully acknowledge the preliminary results on the material fabrication and characterization as well as the printing process from L. Roels and E. Ghys as part of their master's thesis. The authors also thank C. Butnaru from the Materials Engineering department (KU Leuven, Belgium) for her assistance with sample polishing and optical imaging and Dr. Ir. M. Soleimani from Chemelot Research Facilities (Geleen, The Netherlands) for microtoming and electron microscopy imaging.

© 2025 The Author(s). Advanced Functional Materials published by Wiley-VCH GmbH

16163028, 0, Downloaded from https://advanced.onlinelibrary.wiley.com/doi/10.1002/adfm.202512713 by Ku Leuven, Wiley Online Library on [23/09/2025]. See the Terms and Conditions (https://onlinelibrary.wiley.com/terms-and-conditions) on Wiley Online Library for rules of use; OA articles are governed by the applicable Creative Commons License

This work had received funding from the European Research Council (ERC) under the European Union's Horizon 2020 research and innovation programme: Grant Agreement No. 948739 – PEM-Sprint and No. 953348 - ELO-X, the Research Foundation Flanders (FWO) PhD grant No. 1183822N, as well as from Internal Funds KU Leuven under project number STG/20/035.

Conflict of Interest

The authors declare no conflict of interest.

Author Contributions

S.D.S. contributed to conceptualization, investigation, methodology, visualization, and writing - original draft preparation; B.E. to conceptualization, methodology, software, funding acquisition, writing - original draft preparation, and visualization; P.R. to software; P.P. to methodology, writing - review and editing and funding acquisition; F.V.L. to conceptualization and writing - review and editing; and R.C. to conceptualization, supervision, funding acquisition, and writing - review and editing.

Data Availability Statement

The data that support the findings of this study are openly available in KU Leuven RDR at https://doi.org/10.48804/O3PIA6, reference number 59.

Keywords

absorption-dominant, additive manufacturing, conductive polymer composites, EMI shielding, optimization

Received: May 20, 2025
Revised: July 9, 2025
Published online:

[1] K. Ken, M. Rohan, U. David, T. Rick, W. Andrew, *J. Expo. Sci. Environ. Epidemiol.* **2021**, *31*, 585.
[2] J. Miyakoshi, J. C. Lin, M. J. Schoemaker, A. J. Swerdlow, A. W. Preece, N. Leitgeb, K. H. Mild, J. Wilén, P. Bernardi, S. Pisa, M. Cavagnaro, E. Piuzzi, *Advances in Electromagnetic Fields in Living Systems*, Springer New York, NY, **2009**.
[3] B. Chen, Y.-C. Gao, X.-J. Li, Y.-W. Dong, S. Mao, H.-L. Yi, M. Xiong, *2024 Photonics and Electromagnetics Research Symposium (PIERS)*, IEEE, New York **2024**, 1.
[4] S. Grommen, Nucleaire waakhond fanc geeft schoorvoetend toe: kernreactor tihange 3 lag twee weken plat door... een gsm, Available from: https://www.vrt.be/vrtnws/nl/2022/10/18/kernreactor-tihange-3-lag-twee-weken-plat-door-een-gsm/ **2022**, (accessed: April 2025).
[5] S. Sankaran, K. Deshmukh, M. B. Ahamed, S. Khadheer Pasha, *Composites, Part A* **2018**, *114*, 49.
[6] M. Han, Y. Gogotsi, *Carbon* **2023**, *204*, 17.
[7] M. Zhou, Z. Yu, Q. Yan, X. Zhang, *Adv. Funct. Mater.* **2025**, *35*, 2423884.
[8] F. Van Loock, P. Ravichandran, X. Li, P. D. Anderson, R. Cardinaels, *Composites, Part A* **2025**, *191*, 108715.
[9] M. Kamkar, A. Ghaffarkhah, E. Hosseini, M. Amini, S. Ghaderi, M. Arjmand, *New J. Chem.* **2021**, *45*, 21488.
[10] J. Dalal, S. Lather, A. Gupta, R. Tripathi, A. S. Maan, K. Singh, A. Ohlan, *Adv. Mater. Technol.* **2019**, *4*, 1900023.
[11] E. G. B. Dassan, A. A. A. Rahman, M. S. Z. Abidin, H. M. Akil, *Nanotechnol. Rev.* **2020**, *9*, 768.
[12] D. Han, H. Lee, *Curr. Opin. Chem. Eng.* **2020**, *28*, 158.
[13] A. Sang-Joon, L. Howon, C. Kyu-Jin, *Nat. Commun.* **2024**, *15*, 3605.
[14] Y. Danlée, I. Huynen, C. Bailly, *Appl. Phys. Lett.* **2014**, *105*, 123118.
[15] D.-H. Jin, J.-M. Hyun, J.-R. Lee, J.-M. A. and, *Adv. Compos. Mater.* **2024**, *33*, 618.
[16] D. D. Lim, J. Park, J. Lee, D. Noh, J. Lee, J. Choi, W. Choi, *Addit. Manuf.* **2022**, *55*, 102856.
[17] Y. Zhang, H. Li, X. Yang, T. Zhang, K. Zhu, W. Si, Z. Liu, H. Sun, *Polym. Compos.* **2018**, *39*, E671.
[18] W. Cao, X. Li, Y. Chen, L. Jin, R. Guo, N. Song, S. Sun, P. Ding, *Adv. Funct. Mater.* **2025**, *35*, 2406738.
[19] H. Wu, L. Liu, Y. Cai, P. Qian, C. Zhang, B. L. and, *Mater. Technol.* **2022**, *37*, 280.
[20] S. Dang, Y. Lin, X. Wei, H. Ye, *J. Mater. Sci.: Mater. Electron.* **2018**, *29*, 17651.
[21] H. J. Im, J. Y. Oh, S. Ryu, S. H. Hong, *RSC Adv.* **2019**, *9*, 11289.
[22] S. J. Orfanidis, *Electromagnetic Waves and Antennas*, Rutgers University New Brunswick, NJ **2008**.
[23] K. J. Åström, P. Eykhoff, *Automatica* **1971**, *7*, 123.
[24] L. P. Kaelbling, M. L. Littman, A. W. Moore, *J. Artificial Intelligence Res.* **1996**, *4*, 237.
[25] B. Evens, P. Latafat, A. Themelis, J. Suykens, P. Patrinos, *2021 60th IEEE Conference on Decision and Control (CDC)*, IEEE, New York **2021**, 5136.
[26] M. Raissi, P. Perdikaris, G. Karniadakis, *J. Comput. Phys.* **2019**, *378*, 686.
[27] M. Arjmand, M. Mahmoodi, G. A. Gelves, S. Park, U. Sundararaj, *Carbon* **2011**, *49*, 3430.
[28] Y. Bhattacharjee, I. Arief, S. Bose, *J. Mater. Chem. C* **2017**, *5*, 7390.
[29] M. Peng, F. Qin, *J. Appl. Phys.* **2021**, *130*, 225108.
[30] A. N. Vicente, G. M. Dip, C. Junqueira, *2011 SBMO/IEEE MTT-S International Microwave and Optoelectronics Conference (IMOC 2011)*, IEEE, New York **2011**, 738.
[31] F. Van Loock, P. Anderson, R. Cardinaels, *Appl. Math. Modell.* **2024**, *134*, 108.
[32] J. O. Royset, R. J.-B. Wets, *An Optimization Primer*, vol. *440*, Springer, Berlin **2021**.
[33] O. Folorunso, Y. Hamam, R. Sadiku, S. S. Ray, A. G. Joseph, *AIP Conf. Proc.* **2020**, *2289*, 020019.
[34] M. H. Lean, W.-P. L. Chu, *J. Appl. Polym. Sci.* **2016**, *133*, 15.
[35] O. Folorunso, Y. Hamam, R. Sadiku, S. S. Ray, A. G. Joseph, *Polymers* **2019**, *11*, 1250.
[36] D. J. Wales, J. P. Doye, *J. Phys. Chem. A* **1997**, *101*, 5111.
[37] D. Kraft, A software package for sequential quadratic programming, Technical Report DFVLR-FB 88-28, DLR German Aerospace Center – Institute for Flight Mechanics, Koln, Germany **1988**.
[38] S. C. Mun, M. Kim, K. Prakashan, H. J. Jung, Y. Son, O. O. Park, *Carbon* **2014**, *67*, 64.
[39] F. A. Morrison, *Understanding Rheology*, Oxford University Press, Oxford, UK **2001**.
[40] W. Gao, Y. Zheng, J. Shen, S. Guo, *ACS Appl. Mater. Interfaces* **2015**, *7*, 1541.
[41] X. Ji, D. Chen, J. Shen, S. Guo, *Chem. Eng. J.* **2019**, *370*, 1341.
[42] Y.-S. Hong, X.-F. Lu, X.-L. Zhu, K.-L. Zhang, M. Chen, *J. Reinf. Plast. Compos.* **2018**, *37*, 1072.
[43] D. Schmitz, L. Ecco, S. Dul, E. Pereira, B. Soares, G. Barra, A. Pegoretti, *Mater. Today Commun.* **2018**, *15*, 70.
[44] M. Seol, U. Hwang, J. Kim, *Adv. Compos. Hybrid Mater.* **2023**, *6*, 1.
[45] P. Verma, T. Bansala, S. Chauhan, *J. Mater. Sci.* **2021**, *56*, 20.

© 2025 The Author(s). Advanced Functional Materials published by Wiley-VCH GmbH

16163028, 0, Downloaded from https://advanced.onlinelibrary.wiley.com/doi/10.1002/adfm.202512713 by Ku Leuven, Wiley Online Library on [23/09/2025]. See the Terms and Conditions (https://onlinelibrary.wiley.com/terms-and-conditions) on Wiley Online Library for rules of use; OA articles are governed by the applicable Creative Commons License

[46] Z. Xu, T. Dou, Y. Wang, H. Zuo, X. Chen, M. Zhang, L. Zou, *Polymers* **2023**, *15*, 14.
[47] K. Prashantha, F. Roger, *J. Macromol. Sci., Part A* **2017**, *54*, 24.
[48] Z. Li, D. Feng, B. Li, D. Xie, Y. Mei, *Compos. Sci. Technol.* **2023**, *231*, 109803.
[49] S. Lee, D. Kim, N. K. Nguyen, W. Kim, M. Kim, J. Nah, *Carbon* **2025**, *231*, 119759.
[50] B. Park, S. Hwang, H. Lee, Y. Jung, T. Kim, S. J. Kwon, D. Jung, S.-b. Lee, *Adv. Funct. Mater.* **2024**, *34*, 2406197.
[51] B. Sun, S. Sun, P. He, H.-Y. Mi, B. Dong, C. Liu, C. Shen, *Chem. Eng. J.* **2021**, *416*, 129083.
[52] T. Zheng, Y. Yu, H. Lei, F. Li, S. Zhang, J. Zhu, J. Wu, *Adv. Mater.* **2022**, *34*, 2109175.
[53] M. Sala, M. Orfano, V. Secchi, I. Mattei, N. Pianta, V. Zabloudil, C. Lowis, R. Kučerková, M. Nikl, F. Meinardi, E. Auffray, I. Villa, A. Monguzzi, *Adv. Funct. Mater.* **2024**, *35*, 2421434.
[54] J. A. Regenspurg, W. A. Jonkers, M. A. Junker, I. Achterhuis, E. te Brinke, W. M. de Vos, *Desalination* **2024**, *583*, 117693.
[55] F. L. Meng, M. Gao, T. Ding, G. Yilmaz, W. L. Ong, G. W. Ho, *Adv. Funct. Mater.* **2020**, *30*, 2002867.
[56] S. Preechawattanasakul, W. Pivsa-Art, S. Boonyod, S. Pivsa-Art, *Polym. Compos.* **2023**, *44*, 5924.
[57] J. Borges, L. C. Rodrigues, R. L. Reis, J. F. Mano, *Adv. Funct. Mater.* **2014**, *24*, 5624.
[58] J. Smith, Sermoon d1 sprite extruder and cr-10 hotend, Available from: https://www.thingiverse.com/thing:6067494, **2023**, (accessed: April 2025).
[59] S. De Smedt, B. Evens, P. Ravichandran, P. Patrinos, F. V. Loock, R. Cardinaels, Replication data for: "smart stacking: a methodology to produce optimally layered emi shields with maximal green index using fused deposition modeling", https://doi.org/10.48804/O3PIA6, **2025**, (accessed: July 2025).

© 2025 The Author(s). Advanced Functional Materials published by Wiley-VCH GmbH

16163028, 0, Downloaded from https://advanced.onlinelibrary.wiley.com/doi/10.1002/adfm.202512713 by Ku Leuven, Wiley Online Library on [23/09/2025]. See the Terms and Conditions (https://onlinelibrary.wiley.com/terms-and-conditions) on Wiley Online Library for rules of use; OA articles are governed by the applicable Creative Commons License